



Full length article

Segregation engineering of grain boundaries of a metastable Fe-Mn-Co-Cr-Si high entropy alloy with laser-powder bed fusion additive manufacturing



Saket Thapliyal^{a,b}, Priyanshi Agrawal^a, Priyanka Agrawal^a, Saurabh S. Nene^{a,†}, Rajiv S. Mishra^{a,b,*}, Brandon A. McWilliams^c, Kyu C. Cho^c

^a Center for Friction Stir Processing, Department of Materials Science and Engineering, University of North Texas, Denton, TX 76203, USA

^b Advanced Materials and Manufacturing Processes Institute, University of North Texas, Denton, TX 76203, USA

^c Weapons and Materials Research Directorate, CCDC Army Research Laboratory, Aberdeen Proving Grounds, Aberdeen, MD, 21005, USA

ARTICLE INFO

Article history:

Received 9 April 2021

Revised 23 July 2021

Accepted 22 August 2021

Available online 27 August 2021

Keywords:

Grain boundary segregation, Additive manufacturing, Solidification, Alloy design, High entropy alloys, Transformation induced plasticity (TRIP)

ABSTRACT

Laser-powder bed fusion (L-PBF) additive manufacturing offers unprecedented microstructural fine-tuning capabilities. Naturally, benefitting from such capability requires alloys that are amenable to microstructural heterogeneity and hierarchy (MHH) and that exhibit a low hot-cracking susceptibility (HCS). However, columnar growth, which is characterized by capillary effects and poor strain accommodation capabilities, is prevalent in L-PBF and increases the HCS of the processed alloys. Further, while solute segregation is prominent in cellular and dendritic growth modes during L-PBF, the effects of solute segregation on the alloy HCS and L-PBF processing window remain widely unexplored. Here, we demonstrate that solute segregation affects columnar growth, grain coalescence behavior during solidification, MHH and mechanical properties of a metastable $\text{Fe}_{40}\text{Mn}_{20}\text{Co}_{20}\text{Cr}_{15}\text{Si}_5$ (at.%) high entropy alloy (CS-HEA) doped with 0.5 wt.% B_4C (termed CS-BC). A theoretical framework is proposed, which reveals that a boundary-strengthening segregant may reduce the alloy HCS during L-PBF. In as-built CS-BC, boron, a boundary strengthener, segregated to the solidification cell boundaries, whereas carbon remained in the solid solution. The as-built CS-BC exhibited suppressed columnar growth, more random texture, smaller cell size and higher strength as compared to the as-built CS-HEA. Further, a wide crack-free L-PBF processing window of CS-BC allowed fine-tuning of its MHH and thus the mechanical properties. Upon annealing, as carbon-containing precipitates formed, CS-BC exhibited a metastable microstructure and transformation induced plasticity effect, which led to high synergistic strength-ductility. These findings will foster design of alloys that facilitate application-specific manufacture with L-PBF and thus, an extended outreach of L-PBF for structural applications.

© 2021 Acta Materialia Inc. Published by Elsevier Ltd. All rights reserved.

1. Introduction

Precise control systems, and largely varying thermal gradient (G) and growth rate (R) across a small melt pool volume, enable the unprecedented capability of laser-powder bed fusion (L-PBF) to generate hierarchical features (features spanning multiple length scales) and heterogeneous features (features different in phase and/or domains of fine and coarse grains). Notably, solidification parameters G and R control the morphology and size of the microstructural features and hence the variation in these so-

lidification parameters across a solidifying melt pool leads to microstructural heterogeneity and hierarchy (MHH). In L-PBF, these solidification parameters and thus the MHH can be fine-tuned by careful selection of process parameters, such as laser power (P) and scanning speed (v) [1].

While the precise control systems in L-PBF may allow fine-tuning of structural features at near meso or macro length scale, microstructurally flexible and printable materials that facilitate MHH are still required. The features that constitute MHH include grain boundaries, dislocations, solute atoms in solid solution, precipitates, multi-phase microstructure and domains of fine and coarse grains. Non-equiaxial high entropy alloys (HEAs) promise great amenability to such MHH. Reviews by Mishra et al. [2,3] and Nene et al. [4] sum up how fine tuning of composition results in alteration of stacking fault energy and thus activation of deforma-

* Corresponding author.

E-mail address: Rajiv.Mishra@unt.edu (R.S. Mishra).

† Current address: Indian Institute of Technology Jodhpur, Jodhpur, India - 342037.

tion mechanisms, such as transformation induced plasticity (TRIP) in heterophase metastable HEAs. Further, microstructural hierarchy arising from solid solution and precipitates, leads to HEAs exhibiting solid solution [5,6] and precipitation strengthening mechanisms [7–9]. Such hierarchy and heterogeneity in a material results in excellent strength-ductility synergy [10,11]. The state-of-the-art also confirms microstructural hierarchy [9,12,13] and heterogeneity [14–18] in L-PBF processed HEAs. Thus, the unprecedented capabilities of L-PBF to tailor structural features at several length scales combined with hierarchical and heterogeneous microstructure-forming capabilities of HEAs is an intriguing synergy.

Despite the advantages of the L-PBF process, certain disadvantages impale the mechanical properties of the processed alloys and inhibit wider outreach of L-PBF in manufacturing applications. At the outset, while varying G and R in L-PBF are vital for producing MHH, a certain set of thermal gradients and growth rates may exist within the melt pool where columnar growth is favorable [1,19]. Note that such columnar growth may proceed by planar, cellular and/or dendritic growth of the solidification front [19,20]. In L-PBF, increased propensity for columnar growth also arises due to strong thermal gradients directed towards the substrate at the bottom. Competitive growth occurs under such conditions and thus the crystals that have their easy growth directions (along <100> for cubic crystals) aligned with the well-defined thermal gradient, may overcrowd the microstructure. Further, favorable conditions for epitaxial growth within L-PBF may also lead to columnar grains spanning multiple melt pools [21]. Therefore, the process of L-PBF inherently favors columnar growth. Such columnar growth leads to an increased hot cracking susceptibility (HCS) of the material due to capillary effects and poor strain accommodation capability of cells and columnar dendrites during solidification [1,17,22]. Naturally, HEAs are also predisposed to columnar growth upon L-PBF, as reported in myriad works [9,12–18,23,24]. Further, several of these studies also reported microcracks in the as-built microstructure; microcracks indicate poor printability and narrow processing window of the reported alloys [13,15,17,23]. However, the synergistic benefits of microstructurally flexible HEAs and L-PBF can really be enjoyed only when the alloy is printable over a wide range of process parameters, i.e., when the alloy has a wide crack-free L-PBF processing window.

Designing hot cracking-resistant HEAs for L-PBF additive manufacturing, requires comprehensive understanding of factors that affect alloy HCS. To date, several efforts have considered the effect of growth morphology (columnar or equiaxed) on alloy HCS during L-PBF [17,25,26]. However, one factor that may directly affect the grain coalescence behavior during solidification, and yet is seldom considered in current alloy design strategies for L-PBF, is solute segregation. The cellular and dendritic growth that occurs in L-PBF proceeds by the rejection of solute at the intercellular/interdendritic region during the initial stages of solidification, and at grain boundaries during the later stages of solidification (when grains have formed). Such segregation of solute atoms is known to affect the cohesiveness, energy and mobility of the grain boundaries [27–34]. Notably, these characteristics of the grain boundaries determine their strength [27,28,35,36] and coalescence behavior during solidification and thus may affect the HCS [37,38]. Interestingly, efforts to explore the effects of segregation on HCS have commenced; recently it was demonstrated that segregation-induced phase transformation reduces the detrimental effect of residual thermal strain and subsequently reduces the HCS [39]. Worth noting is that the HCS depends on several factors, including thermal strain, solidification growth morphology (columnar or equiaxed), grain size, amount of liquid available for backfilling and the critical temperature range [1]. A paradigm shift in reducing the alloy HCS in L-PBF occurred when alloy design strate-

gies that lead to suppressed columnar growth during L-PBF were implemented [26]. To date, most efforts have used heterogeneous nucleation to suppress columnar growth in L-PBF AM. In this work, we use the concepts from *segregation engineering of grain boundaries* to suppress the inherently occurring columnar growth in L-PBF and simultaneously generate MHH. Concurrently, the effects of solute segregation on alloy HCS, microstructure, and mechanical properties are also assessed. The premises for such concept are, (a) certain elements exhibit high tendencies to segregate at the grain boundaries due to their low solid solubility [28,31,40], (b) solute segregation at the grain boundaries leads to reduced energy and mobility of the boundaries [33,34,41,42], and (c) segregation of the solute may lead to either an enhanced or deteriorated boundary cohesion depending on whether the solute is of strengthening or embrittling type [27,31,35,43]. Based on these premises, alloying elements with high tendencies to segregate at the grain boundaries as well as to enhance grain boundary cohesion are selected; concomitantly, boundary energy and mobility would also reduce. The stabilization and enhanced cohesion of boundaries may lead to suppressed columnar growth, and fine-grained microstructure. Additionally, an enhanced solid solution and boundary precipitation may add to the MHH of the alloy and thus may improve alloy strength. A theoretical framework is proposed that describes how solute segregation may directly affect the alloy HCS. Insights on implementing the concepts from *segregation engineering of boundaries* into strategies for design of printable and high strength alloys for L-PBF are also provided. This work uses L-PBF AM because: a) it is a rapid solidification technique that leads to cellular and/or dendritic growth characterized by segregation, and b) it leads to variation in solidification parameters (G and R) across a small melt pool volume. While the former attribute of L-PBF allows for implementation of segregation engineering, the latter allows generation of microstructural hierarchy and heterogeneity. Note that other rapid solidification processing routes, such as direct energy deposition (DED) and electron beam melting (EBM), also lead to segregation and variation in solidification parameters (G and R) within a small volume (melt pool). Therefore, this work may also be extended to EBM and/or DED processing routes.

2. Methods

2.1. Implementing segregation engineering in L-PBF

Boron and carbon have a strong tendency to segregate at the grain boundaries in Fe [43–47]. The segregation of these elements results in reduced grain boundary energy [44,47–50], enhanced cohesion of the grain boundaries [36,44,51,52] and thus, strengthening of the grain boundaries [52,53]. Therefore, a non-equiautomatic metastable $F_{40}Mn_{20}Co_{20}Cr_{15}Si_5$ (at.%) HEA (referred to as CS-HEA) powder was doped with 0.5 wt.% B_4C powder (termed CS-BC hereafter) and processed with L-PBF bearing in mind the following implications:

- Boron may segregate towards the boundaries and lead to reduced boundary energy [30,36,41,42] and mobility as well as enhanced boundary cohesion [30,32,33,35,41,54]. Consequently, such effects may suppress thermal gradient-driven columnar growth in L-PBF and enhance grain boundary strength [36,41].
- Boron segregation at the grain/cell boundaries may result in formation of borides at these boundaries and thus, lead to boundary pinning and suppression of columnar growth during solidification. Formation of borides would also add to the MHH.
- Similar to the effects of boron addition as mentioned in (a), carbon may segregate to boundaries and aid in suppressed columnar growth, enhanced boundary cohesion, and enhanced grain

Table 1
Chemical composition of the pre-alloyed CS-HEA powder.

Element	Fe	Co	Mn	Cr	Si
Nominal (at.%)	40	20	20	15	5
Actual (at.%)	41.8 ± 1.1	19.1±1.2	18.8 ± 1.1	14.8±1.0	5.5±0.4

Table 2
L-PBF process parameters used in this work.

Parameter/specimen ID	Laser power(W)	Scan speed (mm/s)	Layer thickness (mm)	Hatch distance(mm)	Scan strategy
100-800	100	800	0.04	0.10	Stripes with 67° inter-layer rotation
120-800	120	800			
120-1000	120	1000			
150-800	150	800			

boundary strength [35,36]. Additionally, carbon may also stabilize γ -f.c.c. [55–60].

d) Carbon segregation at the boundaries may result in formation of carbides and thus pin grain and/or cell boundaries and consequently suppress columnar growth during solidification. Formation of carbides would also add to the MHH.

In addition to points (a) – (d), the presence of undissociated B_4C particles in the L-PBF processed CS-BC is also considered. Scheil-Gulliver solidification simulations (SGSS) performed using Thermo-Calc software were used to predict the solidification path of CS-HEA and CS-BC. Exploiting concepts from segregation engineering of grain boundaries in L-PBF AM was expected to facilitate MHH, suppress cracking-susceptible columnar growth and lead to good printability at a wide range of process parameters. The MHH and good printability result in good mechanical properties whereas a wide processing window is needed to tailor MHH and thus the mechanical properties.

2.2. Experimental methods

CS-HEA was gas-atomized at Oerlikon Metco such that the D_{90} value was $\sim 48 \mu\text{m}$ (chemical composition provided in Table 1 [18]). To investigate the effects of B_4C addition on the microstructure and mechanical properties of CS-HEA, the process of L-PBF was conducted in two rounds: The first round featured L-PBF of virgin CS-HEA powders; the second round involved L-PBF of pre-mixed powder of CS-BC. To prepare the CS-BC powder, CS-HEA powder was doped with 0.5 wt.% B_4C powder (average particle size $\sim 6 \mu\text{m}$), and the mixture was placed on a high-speed rolling mixer for ~ 72 hours to achieve thorough mixing. A top-down view of several reconstructed X-ray microscope images of the B_4C doped CS-HEA powders are shown in the Supplementary video S1. The Aconity MIDI L-PBF system equipped with a fiber laser was used for processing; laser was operated in continuous wave mode with a spot size of $80 \mu\text{m}$.

Table 2 lists the L-PBF process parameters used in this work. Note that CS-HEA was processed only at the parameter ID 120-800 (adapted from our recent work on CS-HEA [18]), whereas CS-BC was processed at all parameters listed in Table 2. To investigate the effect of B_4C addition, microstructural and mechanical properties of CS-HEA and CS-BC specimens processed at the same parameters (ID 120-800 in Table 2) were compared. L-PBF was performed in an Ar atmosphere with oxygen content maintained below 100 ppm. Rectangular blocks of dimension $35 \times 15 \times 10 \text{ mm}^3$ were fabricated, and the dimensions were kept constant across the alloy compositions and process parameters reported in this work.

To assess the processing window, all CS-BC specimens were inspected for cracks using X-ray microscopy (XRM). A constant volume of $1.5 \times 1 \times 3 \text{ mm}^3$ was scanned with a Zeiss Xradia 520 Versa X-ray microscope. The X-ray source power and voltage were

set to 10 kW and 160 kV, respectively, and a 4X objective was used. The binning value and voxel size were set to 2 and $1.6 \mu\text{m}$, respectively; 2401 projections were acquired for each specimen. ORS Dragonfly software was used for image processing.

Specimens for scanning electron microscopy (SEM) and orientation imaging microscopy (OIM) were machined from the rectangular blocks using electro-discharge machining (EDM). Surfaces from these specimens containing the build direction were polished to $0.02 \mu\text{m}$ surface finish. FEI Nova nano SEM equipped with a Hikari electron backscattered diffraction (EBSD) detector was used. ImageJ was used for image analysis of SEM micrographs, whereas TSL OIM was used for EBSD data analysis.

FEI Nova 200 NanoLab focused ion beam milling setup was used to prepare CS-BC 120-800 specimens for transmission electron microscopy (TEM) and energy dispersive x-ray spectroscopy (EDS) analysis. TEM and EDS analysis was then performed using G2 F20 S-Twin 200 keV FE-STEM. TEM-based orientation imaging microscopy, also referred to as precession electron diffraction (PED), was performed to characterize the nanoscale phases. TOPSPIN software was used for data acquisition and ACOM software was used for analysis of the PED data.

Mechanical characterization was performed using a mini tensile machine. Tensile specimens of gage length and width 5 mm and 1.25 mm, respectively, were machined using EDM such that the gage width for all the specimens was along the build direction. Machined mini tensile specimens were then polished down to 1.2 mm thickness and final surface finish of $1 \mu\text{m}$. Three tensile specimens were tested for each specimen condition. Tensile tests were performed at room temperature at an initial strain rate of 10^{-3} s^{-1} .

3. Results

3.1. As-built microstructure

Fig. 1 shows the SGSS generated temperature (T) vs mole fraction of solid (F_s) curves and solidification paths for CS-HEA and CS-BC. The solidification path suggests the formation of borides and carbides in CS-BC starting at $F_s \sim 0.72$. Considering the high tendencies of B and C to segregate at the boundaries, these phases may form at the cell and/or grain boundaries during solidification. Such phases not only add to the hierarchy of microstructure but may also pin the boundaries. The T- F_s curves also reveal smaller critical temperature range (CTR) of CS-BC ($\sim 110^\circ\text{C}$) as compared to CS-HEA ($\sim 280^\circ\text{C}$). CTR is defined as the difference between temperatures corresponding to the F_s value of 0.95 ($T_{F_s=0.95}$) and 1 ($T_{F_s=1}$) (Eq. (1) [61]).

$$CTR = T_{F_s=0.95} - T_{F_s=1} \quad (1)$$

A higher value of CTR indicates higher HCS of an alloy. In the terminal stage of solidification ($F_s > 0.9$), solidification and thermal

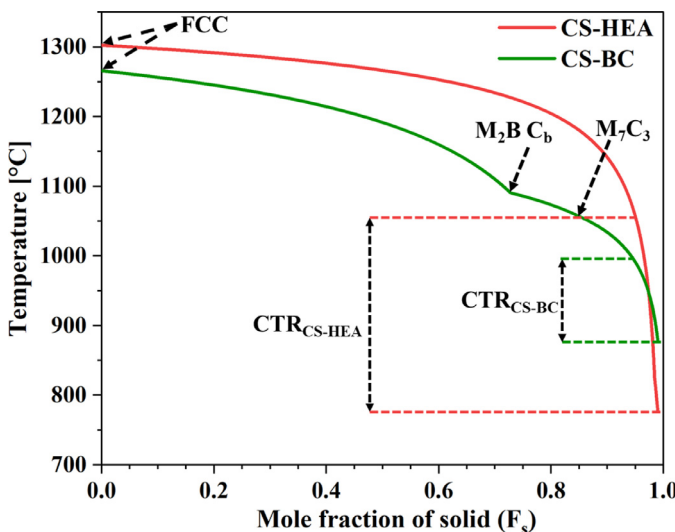


Fig. 1. Scheil-Gulliver solidification behavior of CS-HEA and CS-BC. T-F_s curves depicting solidification path for CS-HEA and CS-BC.

shrinkage effects exert strains on the concomitantly bridging grains that have not yet developed significant ductility to accommodate such strains. Grains do not develop ductility until very late stages in solidification ($F_s \sim 0.98$ [62]) and a higher value of CTR indicates that the alloy spends more time in this brittle stage. Further, linear thermal shrinkage increases directly with temperature difference; in the terminal stage, this temperature difference corresponds to the CTR [22,63,64]; a high CTR therefore indicates high HCS of the alloy.

A stark columnar growth alongside a strong cubic texture of f.c.c. grains is indicated in the inverse pole figure (IPF) map (Fig. 2(a)) and pole figure (Fig. 2(b)) of the CS-HEA specimen. Evidently, the addition of B₄C results in a heterogeneous grain structure with regions of fine and coarse grains (Fig. 2(c)) and weakening of the cubic texture in f.c.c. grains within the CS-BC 120-800 specimen (Fig. 2(d)). Figs. 2(e) and 2(f) represent the grain shape aspect ratio (GSAR) maps for the as-built CS-HEA and CS-BC 120-800 specimens, respectively. The GSAR has been defined as the ratio of the minor axis to the major axis of ellipses that are best fitted to the grains. The GSAR maps reveal suppressed columnar growth in CS-BC specimen as the fraction of grains with an aspect ratio ≤ 0.3 , is only ~ 0.21 in CS-BC compared to 0.48 in CS-HEA. Figs. 2(g) and 2(h) represent the phase maps for the CS-HEA and the CS-BC 120-800 specimens, respectively. The phase fraction of γ -f.c.c. increases from 0.26 in CS-HEA specimen to 0.98 in the CS-BC 120-800 specimen. Next, cell sizes were calculated for as-built CS-HEA and CS-BC 120-800 specimens. The linear intercept method was implemented, and SEM micrographs acquired at different magnifications were used to calculate cell size. The average cell size for CS-HEA was $\sim 616 \pm 35$ nm. The CS-BC specimen on the other hand exhibited a finer cell size of $\sim 480 \pm 47$ nm.

High-angle annular dark-field scanning-TEM (HAADF-STEM) image in Fig. 3(a) and the EDS map in Fig. 3(b) confirm the segregation of B at the cell boundaries in as-built CS-BC 120-800 specimen. At the cell boundaries, Mn- and Cr-rich zones are also seen in Figs. 3(g) and 3(h), respectively. Few precipitates are seen at the cell boundaries (Fig. 3(a)); considering the segregation pattern in the EDS maps and the solidification path (Fig. 1), these precipitates may be borides. Note that the solidification path shown in Fig. 1 predicts formation of M_2B type borides, where M may represent Cr and/or Mn [65,66]. However, as compared to Mn, Cr has a higher tendency to form borides in Fe-based alloys [67]. A detailed discussion on these precipitates is provided in Section 4.3.

Uniform distribution of C is also evident (Fig. 3(c)), and points towards retention of C in solid solution.

Bright field TEM (BFTEM) images in Figs. 4(a) and 4(b) correspond to as-built CS-HEA (zone axis along [011]) and the CS-BC 120-800 (zone axis along [001]) specimens, respectively. The diffraction patterns (DPs) in the inset confirm that both images were acquired from γ -f.c.c. phase regions. Twins are prominent in the CS-HEA specimen and stacking faults are also seen, whereas a high density of intersecting stacking faults is evident in the CS-BC specimen.

3.2. L-PBF processing window of CS-BC and its microstructural implications

Figs. 5(a)-(d) show the 2D slices acquired from XRM of different as-built CS-BC specimens (build direction is along the vertical axis of images). The corresponding 3D reconstructed volumes from different CS-BC specimens are also provided in supplementary Figs. S1(a)-(d). XRM revealed absence of cracks at all process parameters; this indicates a wide crack-free processing window of CS-BC with L-PBF. However, irregularly shaped lack of fusion (LOF) pores were still observed in specimens processed at smallest power and fastest scanning speed (Figs. 5(a)-(b)). In L-PBF, such pores are common when the energy available for melting is insufficient. Features resembling the powder particles in Figs. 5(a)-(b) are common types of LOF defects found in L-PBF [68,69]. Contrarily, spherical pores were observed in 120-800 (Fig. 5(c)) and 150-800 (Fig. 5(d)) specimens.

A subsequent comparison of grain size of CS-BC specimens processed at different parameters is shown in Fig. 6. The IPF maps and corresponding phase maps are provided in supplementary information Figs. S2(a)-(f). Different grain size distribution can be obtained at different process-parameters, which is important for fine-tuning the mechanical properties. Grain size distribution shifts towards the coarser side with increasing laser power (Fig. 6). For the same laser power, the specimen with a lower scanning speed exhibits a coarser distribution. As for phase distribution, all CS-BC specimens exhibited a γ -dominant microstructure (Table 3, Fig. 1(h), and supplementary Figs. S2(b), (d), and (f)).

3.3. Mechanical behavior of as-built specimens

Fig. 7(a) shows the tensile engineering stress vs engineering strain curves for the as-built CS-HEA and the 120-800 CS-BC specimens. Phase maps acquired from the respective fractured specimens are also presented. Addition of B₄C increased yield strength (YS) from $\sim 550 \pm 16$ MPa to $\sim 915 \pm 21$ MPa and the ultimate tensile strength (UTS) from $\sim 980 \pm 28$ MPa to over ~ 1200 MPa. The phase maps acquired from the fractured gage area containing loading direction reveal considerably high deformation induced $\gamma \rightarrow \varepsilon$ transformation in CS-HEA as compared to CS-BC (Figs. 2(g)-(h) and 7(a)). Fig. 7(b) shows very high initial work hardening rate (WHR) in as-built CS-BC 120-800 specimen. However, unlike the as-built CS-HEA specimen, this WHR could not be sustained until the later stages of plastic deformation in the CS-BC specimen. Consequently, the as-built CS-HEA specimen exhibited high elongation to failure (EF) of over $\sim 24\%$ as compared to a modest EF of $\sim 5.6 \pm 0.3\%$ in CS-BC. Fig. 7(c) reveals the tensile properties of the different CS-BC specimens as listed in Table 2. The highest YS of over 1 GPa was obtained for the specimen processed at highest scanning speed (specimen ID 120-1000) and was followed by that of the specimen processed at lowest power (specimen ID 100-800). Contrarily, the specimen processed at highest laser power (specimen ID 150-800) exhibited lowest YS and highest EF. As for the deformation induced transformative behavior, just as the 120-800 CS-BC specimen (Fig. 7(a)), the microstructure of all other CS-BC specimens

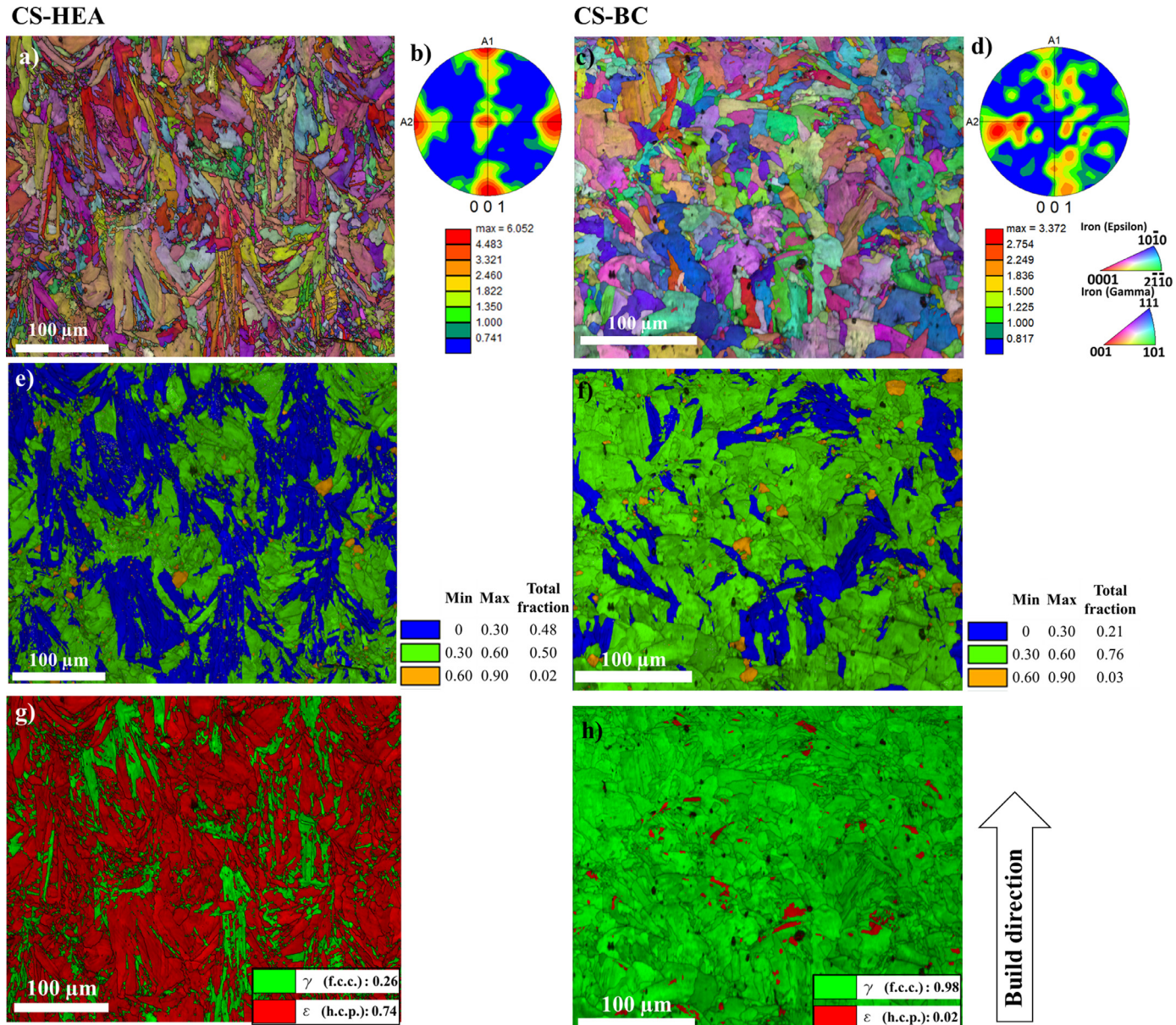


Fig. 2. EBSD measurements depicting suppressed columnar growth and γ -f.c.c. dominant microstructure within as-built CS-BC as compared to CS-HEA. (a) IPF map, (b) pole figure, (e) GSAR map, and (g) phase map for as-built CS-HEA 120-800 specimen. (c) IPF map, (d) pole figure, (f) GSAR map, and (h) phase map for as-built CS-BC 120-800 specimen.

Table 3
Phase fractions in undeformed specimens of as-built CS-HEA and CS-BC.

Specimen	CS-HEA (120-800)	CS-BC (120-800)	CS-BC (100-800)	CS-BC (120-1000)	CS-BC (150-800)
γ -f.c.c. phase fraction	0.26	0.98	0.97	0.97	0.96
ε -h.c.p. phase fraction	0.74	0.02	0.03	0.03	0.04

remained γ -f.c.c. dominant upon deformation and thus, TRIP effect could not be activated; this reduced the EF of all the CS-BC specimens as compared to the as-built CS-HEA. The enhanced stability of γ phase and the subsequent suppression of TRIP effect in as-built CS-BC specimens is discussed next and in more detail in Section 4.

3.4. Annealing of CS-BC 120-800 specimen

The microstructural and mechanical characteristics reported thus far, have revealed high stability of γ -f.c.c. phase, suppres-

sion of TRIP effect and subsequent loss of ductility in the as-built CS-BC HEA. Bearing in mind that the TEM EDS maps indicated retention of C in solid solution (Fig. 3(c)) and that C is a γ -stabilizer [55–59], its depletion from the solid solution to form precipitates could reduce the stability of γ phase [70] and lead to a dual phase microstructure (containing γ and ε phases) within the CS-BC 120-800 specimen. Further, the C-depleted solid solution may lead to a metastable γ phase (as in CS-HEA) and thus, trigger the deformation induced phase transformation within the CS-BC HEA. Such microstructural heterogeneity and hierarchy may enhance the ductility of CS-BC. In view of these considerations,

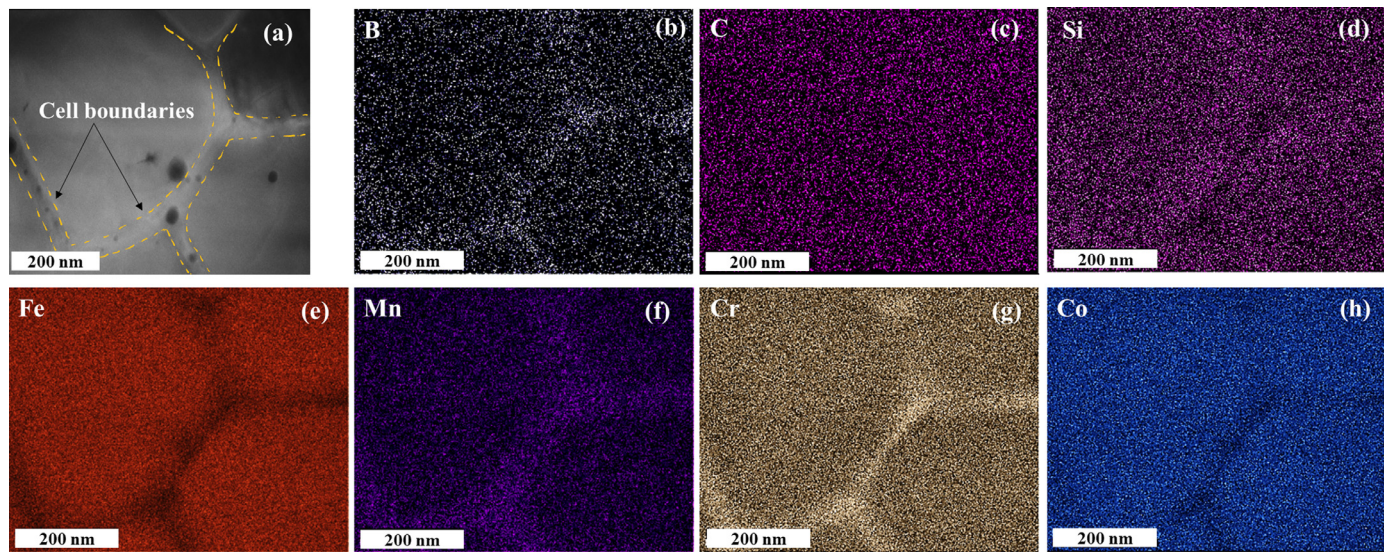


Fig. 3. Segregation behavior at the cell boundaries in as-built CS-BC 120-800 specimen. (a) HAADF-STEM image and (b-h) corresponding EDS maps depicting elemental distribution.

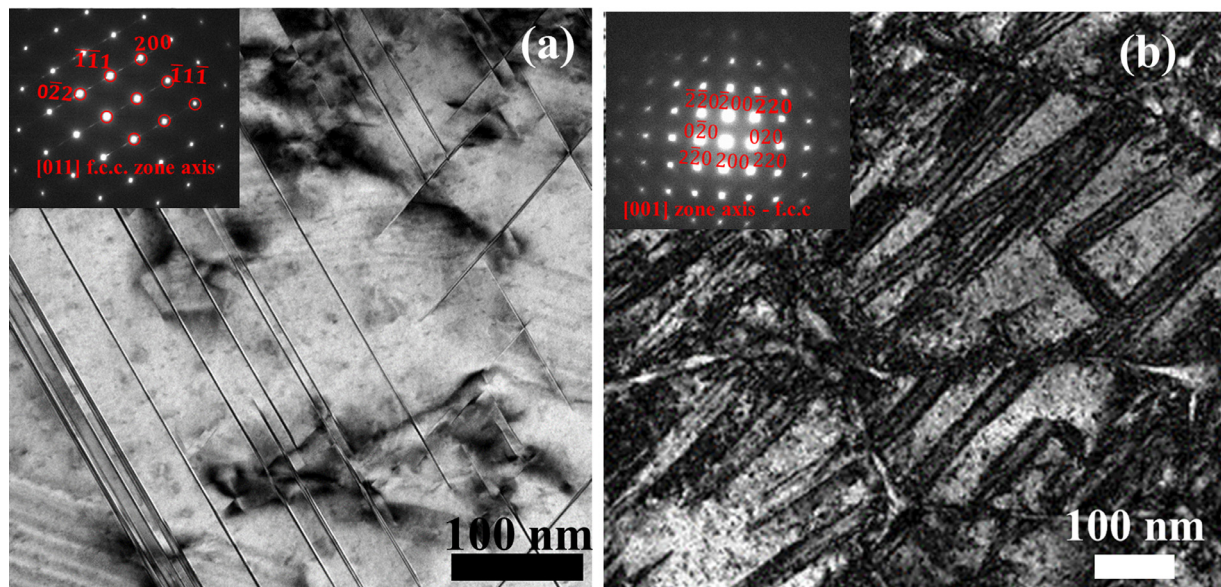


Fig. 4. Twins and stacking faults in as-built specimens. BFTEM images showing (a) twins in CS-HEA ($[011]$ beam direction), and (b) high density of intersecting stacking faults within the cells in the CS-BC 120-800 specimen ($[001]$ beam direction). Corresponding DPs are shown in the inset.

the annealing of the 120-800 specimen of CS-BC was performed at 900°C for 10 minutes. Figs. 8(a) and 8(b) show backscattered electron (BSE) images for as-built and annealed CS-BC 120-800 specimens, respectively. With SEM level resolution, any precipitation at grain and cell boundaries was not evident in the as-built specimen; however, annealing resulted in evident precipitation at these boundaries. Fig. 8(c) is an EBSD phase map overlaid on the image quality map; the EBSD measurements were acquired from the same area as shown in Fig. 8(b). The yellow encircled regions in Figs. 8(b) and 8(c) show a common and easily identifiable feature in both figures. Certain cells and grains that had their boundaries “decorated” with precipitates (Fig. 8(b)), exhibited ε -dominant microstructure, whereas the ones that did not reveal prominent precipitation mostly exhibited a γ -dominant microstructure.

A detailed TEM characterization was performed to determine the elemental composition as well as the crystal structure of the second-phase precipitates seen on the cell boundaries of the ε -

h.c.p. region upon annealing. Characterizing these precipitates is important for determining if depletion of C from the solid solution and subsequent formation of C-containing second phase precipitates occurred at all. Depletion of C from solid solution to form second phase precipitates would explain the reduced stability of γ -f.c.c. phase upon annealing. Fig. 9(a) represents a weak beam dark-field TEM micrograph ($[10\bar{1}0]$ zone axis) acquired from the annealed CS-BC 120-800 specimen; precipitates were clearly seen “decorating” the cell-boundaries. Figs. 9(b)-(h) show the corresponding EDS maps acquired from the red highlighted region of Fig. 9(a). The precipitates evident on the cell boundaries were rich in Cr, B and C; thus, the EDS maps revealed the depletion of C from the solid solution within as-built CS-BC. BFTEM and PED were performed to further characterize the cell boundary precipitates and the features constituting the MHH in annealed CS-BC 120-800 specimen. The BFTEM image and PED map were acquired from the same red highlighted region in Fig. 9(a). Fig. 9(i) shows

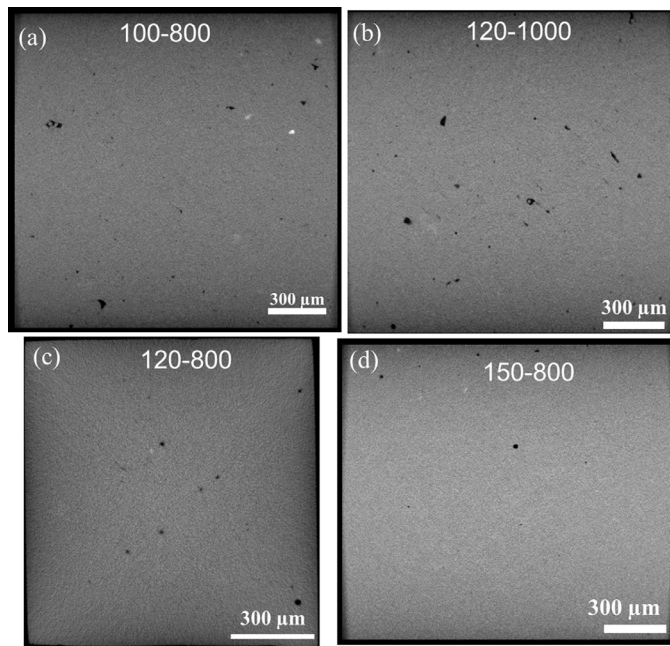


Fig. 5. XRM of as-built CS-BC specimens. (a)–(d) 2D slices obtained from different CS-BC specimens; images are labeled with corresponding specimen ID.

the BFTEM image with zone axis along [10̄10]; the corresponding DP is also shown in Fig. 9(j). Notably, intersecting stacking faults were still seen in annealed condition (Fig. 9(i)). PED phase map alongside DPs from matrix and different precipitates are shown in Fig. 9(k). Based on the elemental distribution obtained from the EDS maps in Figs. 9(b)–(d), the precipitates in the PED map were established as C-, B- and/or Cr-rich. Further, PED phase map revealed that these precipitates were orthorhombic and hexagonal borides, and hexagonal carbides embedded in the ε -h.c.p. matrix. Therefore, the EDS and PED maps reaffirmed the stabilization of ε phase with precipitation of C- and B-containing secondary phases in the annealed CS-BC 120-800 specimen. An equilibrium phase diagram provided in supplementary Fig. S3 also predicts the formation of M_7C_3 type carbides and M_2B type orthorhombic borides. Overall, the TEM EDS maps, the PED map and the calculated equilibrium phase diagram revealed that the precipitates formed were C-, B- and Cr-rich and that these precipitates may be orthorhombic and hexagonal Cr_2B and hexagonal Cr_7C_3 .

3.5. Mechanical behavior of the annealed CS-BC 120-800 specimen

Fig. 10(a) shows the engineering stress vs. engineering strain curve for the annealed CS-BC 120-800 specimen. While annealing reduced the YS of the CS-BC 120-800 specimen from ~915 MPa to ~690 MPa, its UTS (~1180 MPa) remained almost equal to or even higher than the as-built CS-BC specimens (Fig. 7(c)). A stark contrast with the as-built CS-BC specimens was seen in terms of the total EF; for the annealed specimen, it increased to ~17±1.2%, i.e., an increase of over 150% from the highest EF in as-built condition (Fig. 7(c)). Another contrast with the as-built CS-BC 120-800 specimen occurred in terms of WHR, as evident from the comparison of Fig. 10(b), which shows the WHR vs true strain curve for annealed 120-800 specimen, and Fig. 7 (b). As compared to the as-built CS-HEA specimen (Fig. 7(a)), the YS and UTS of the annealed CS-BC specimen increased by ~130 MPa, and ~200 MPa, respectively, while the total EF in the annealed CS-BC specimen is still lower than that of the as-built CS-HEA. The EBSD-generated phase map (Fig. 10(c)) was acquired from the gage area of the fractured specimen. Upon deformation, the γ phase fraction reduced from 0.65 (Fig. 8(c)) to 0.24 (Fig. 10(c)); this indicates deformation induced $\gamma \rightarrow \varepsilon$ phase transformation in the annealed CS-BC 120-800 specimen.

4. Discussion

4.1. Implications of boundary segregation for columnar growth and alloy HCS in L-PBF

An interface consists of dangling bonds, and thus, exhibits a higher free energy than the rest of the solid. Before solidification, the interfacial energy is equal to the interfacial energy of the solid-liquid interface (γ_{SL}), whereas upon complete solidification, this interfacial energy manifests as the grain boundary energy (γ_{GB}). As the solute atoms segregate towards the interfaces, the interfacial energy is reduced as a result of Gibbsian adsorption [28,40,41,71]. This reduction in interfacial energy upon segregation serves as the driving force for segregation [41,42]. The suppressed cubic texture (Fig. 2(d)), the suppressed columnar growth (Fig. 2(f)), and reduced cell size in CS-BC altogether corroborate the reduced interfacial energy and mobility of the boundaries in CS-BC. The solute segregation towards the boundaries (Fig. 3) results in such effects [28,30,33,34,41,47,49,50,71]. The reduced energy and mobility of the boundaries have significant implications for L-PBF AM. One

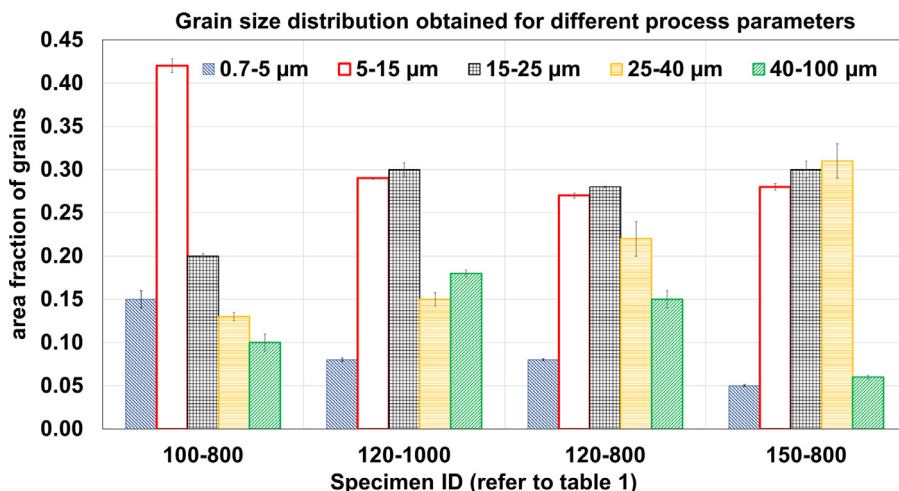


Fig. 6. The attributes of MHH can be fine-tuned for an alloy with wide processing window. The variation in grain size distribution in CS-BC specimens printed at different parameters can be noted.

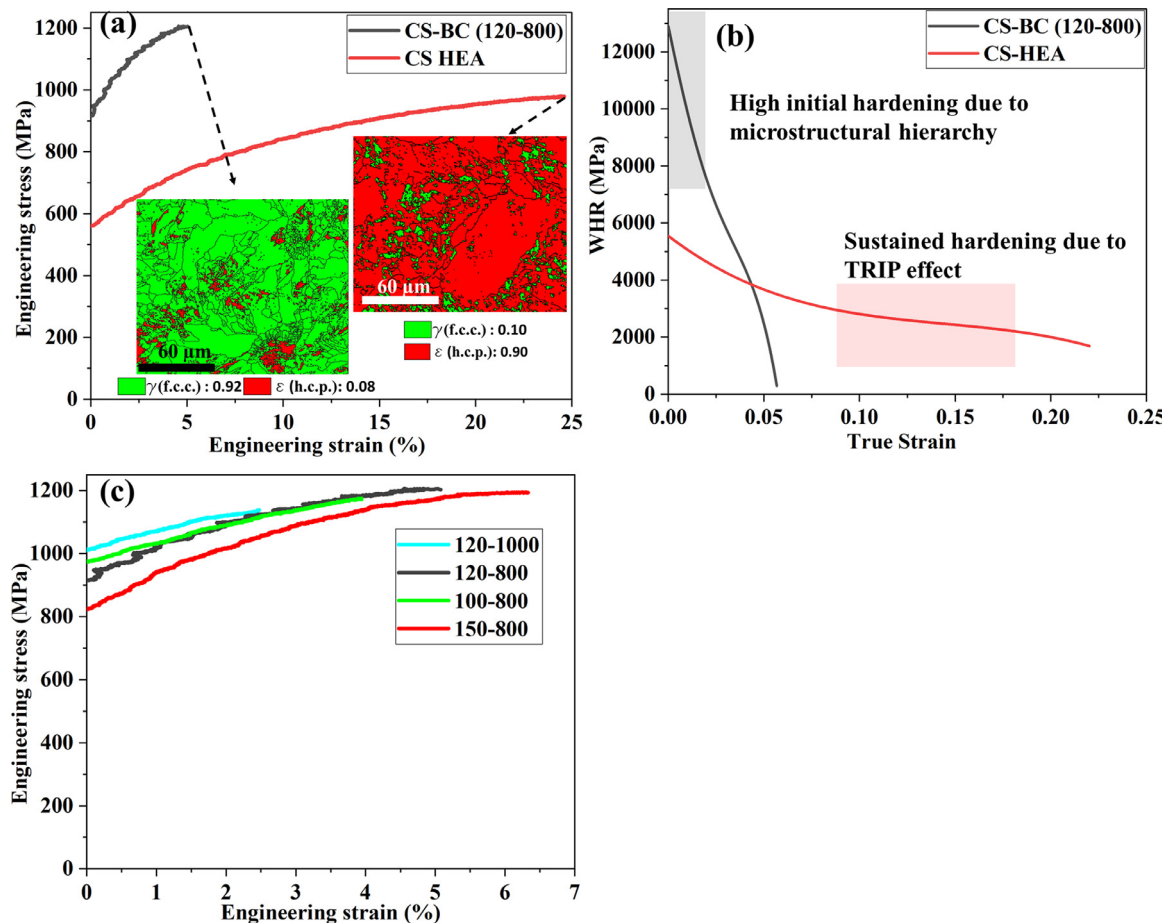


Fig. 7. Tensile deformation behavior of as-built CS-BC and CS-HEA specimens. (a) Engineering stress vs. engineering strain curves for as-built CS-HEA and CS-BC 120-800 specimen alongside the phase maps acquired from their fractured specimens. (b) Work hardening response of CS-HEA and CS-BC 120-800 specimen. (c) Engineering stress vs. engineering strain curves for different CS-BC as-built specimens.

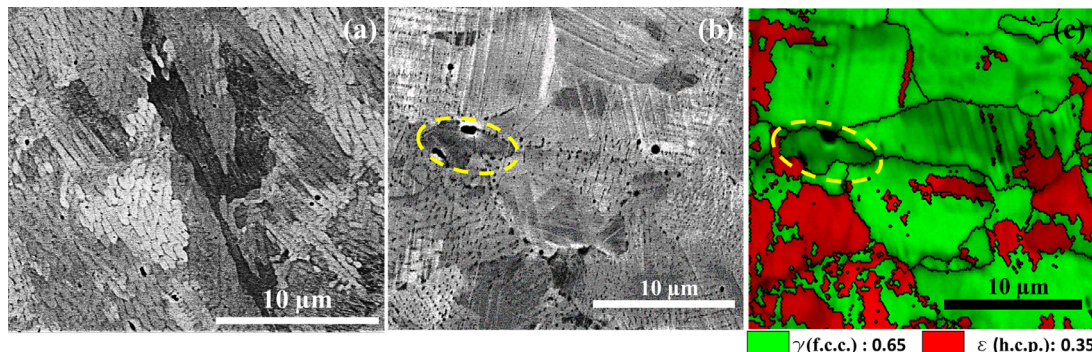


Fig. 8. Correlating γ phase stability with the cell and grain boundary precipitation behavior in CS-BC 120-800 specimen. (a) SEM micrograph of an as-built CS-BC depicting no cell and grain boundary precipitation. (b) SEM micrograph of an annealed CS-BC specimen with evident cell boundary precipitation within certain grains, and (c) corresponding EBSD phase map showing phase evolution with precipitation.

such implication is grain refinement through reduced propensity of grain growth in the direction of maximum thermal gradient. Elaborating, the driving force for grain growth is, reducing the interfacial energy, i.e., certain larger grains grow at the expense of smaller grains to reduce the overall interfacial energy. While adsorption of solute atoms at the boundaries leads to reduced interfacial energy of the boundaries, and thus, reduced driving force for grain growth [28,40–42,44,71], the solute drag effect further leads to reduced mobility of the boundaries [33,34,72]. Cooperatively, both these effects lead to microstructural refinement in as-built CS-BC. Further, during solidification, reduced interfacial energy and mobility of the

boundaries will prevent growth of crystals that have their direction of easy growth ($<100>$ in case of cubic materials) oriented in the direction of strong thermal gradients in L-PBF. Subsequently, more unfavorably oriented crystals are likely to grow and thus, result in a more random texture (Fig. 2(d)).

Another significant implication of reduced interfacial energy and mobility through boron segregation for L-PBF is reduced HCS of an alloy. One way in which the HCS is reduced is by suppressed columnar growth. To avoid hot cracks, solidification shrinkage must be compensated by liquid flow in the interdendritic region, which is similar to a capillary channel. Pressure differential between the

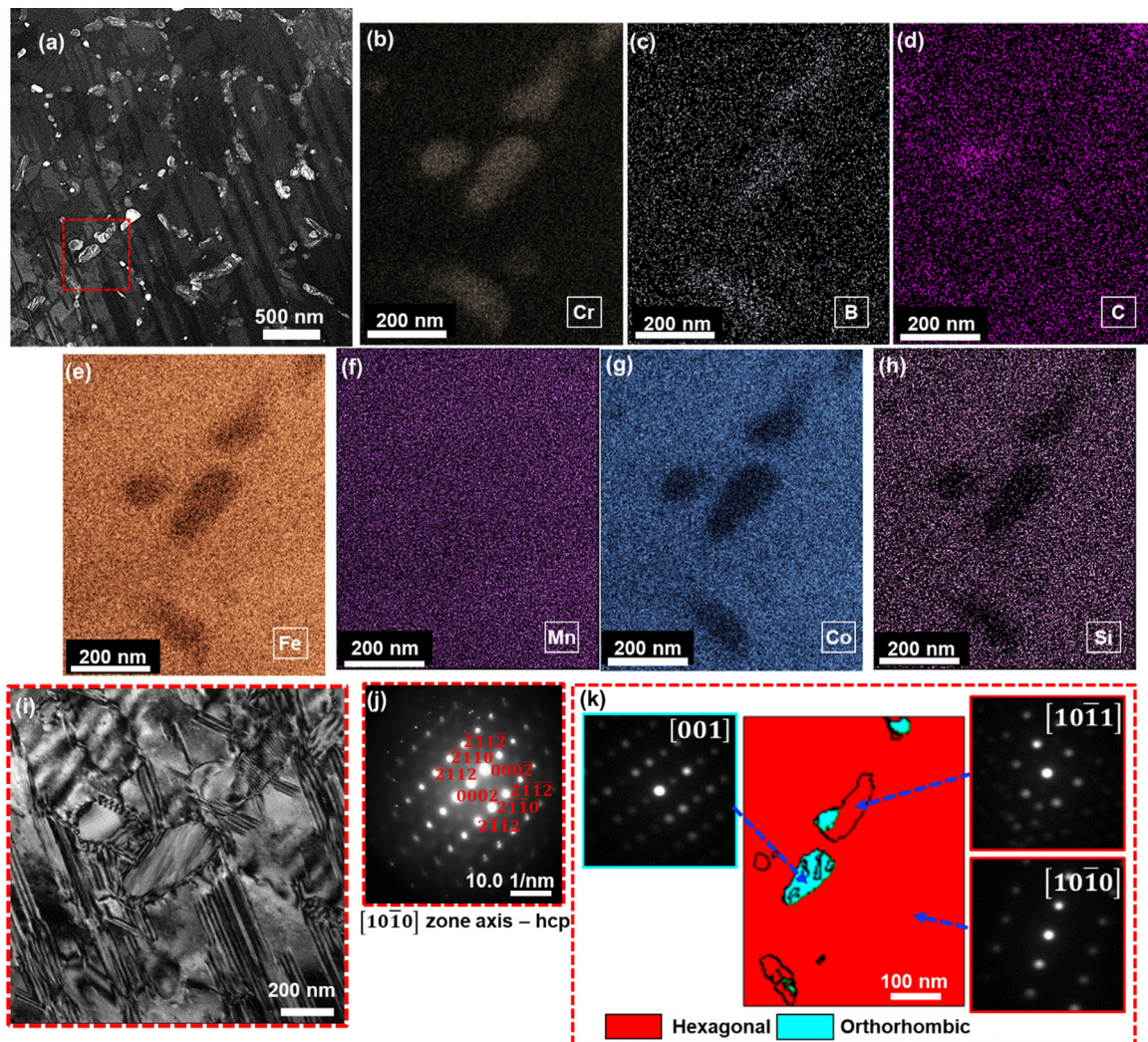


Fig. 9. Cell boundary precipitates, elemental distribution, stabilized ε -h.c.p. phase, and stacking faults in an annealed CS-BC 120-800 specimen. (a) Dark-field TEM image and (b-h) corresponding EDS maps acquired from the red highlighted area in (a). Also captured from the red highlighted area in (a) are: (i) BFTEM image and (j) corresponding DP, (k) PED phase map and DPs from different regions as indicated by blue dashed arrows. (For interpretation of the references to colour in this figure legend, the reader is referred to the web version of this article.)

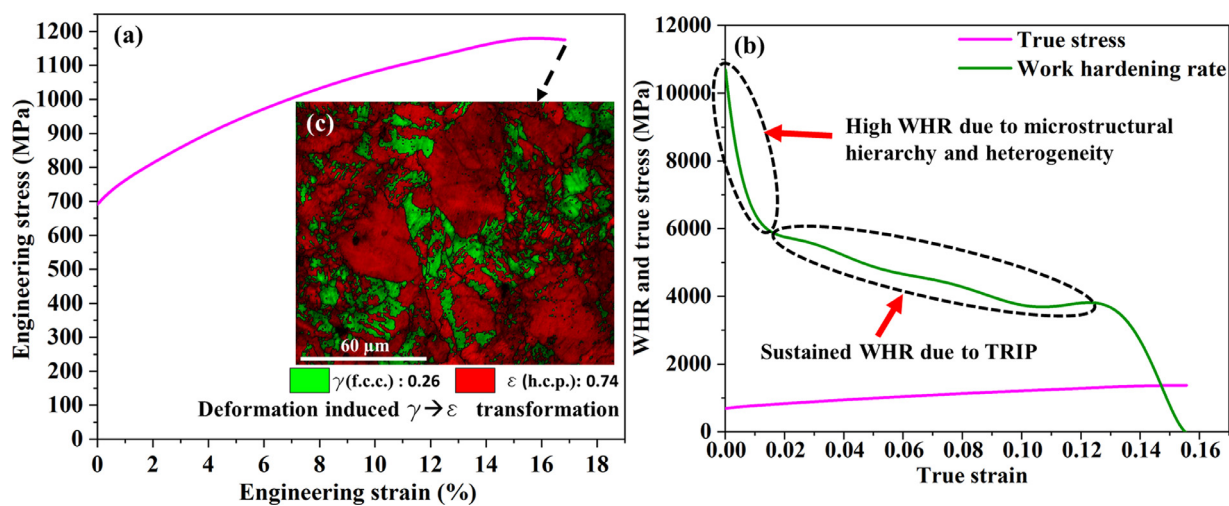


Fig. 10. Tensile deformation behavior of annealed CS-BC 120-800 specimen. (a) Engineering stress vs engineering strain curve (b) Work hardening response and (c) EBSD phase map showing phase evolution upon fracture.

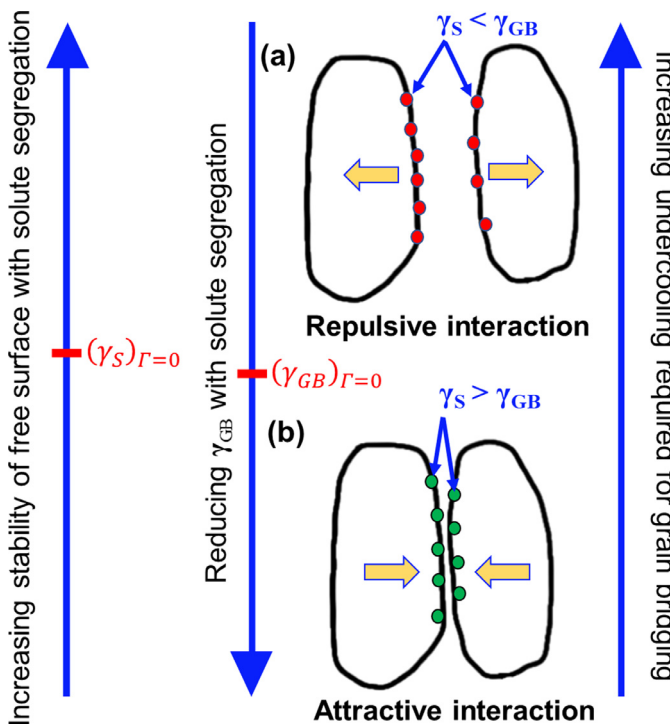


Fig. 11. An illustration depicting possible effects of solute segregation on interfacial energies and solidification behavior of an alloy. $(\gamma_s)_{\Gamma=0}$ and $(\gamma_{GB})_{\Gamma=0}$ are arbitrary representations of the free surface energy and grain boundary energy of a pure metal, respectively. Further, an increasing stability of a free surface is equivalent to a decreasing free surface energy. (a) A segregant of embrittling type (shown in red circles) may decrease the free surface energy (γ_s) and increase the grain boundary energy (γ_{GB}) of an alloy and, thus, may increase the undercooling required for bridging of the two solidifying boundaries. Due to segregation of an embrittling solute, a repulsive type of interaction is energetically favored when γ_s becomes less than γ_{GB} . Subsequently, grain bridging is delayed to a later stage in solidification; this increases the alloy HCS. (b) Conversely, segregant of strengthening type (shown in green circles) may decrease γ_{GB} and increase γ_s of an alloy and, thus, may reduce the undercooling required for bridging of the two solidifying boundaries. Due to segregation of a strengthening solute, an attractive type of interaction between the two solidifying boundaries is energetically favored when γ_{GB} becomes less than γ_s . Subsequently, grain bridging or coalescence occurs at a lower undercooling and at an earlier stage in solidification; this reduces the alloy HCS. (For interpretation of the references to colour in this figure legend, the reader is referred to the web version of this article.)

dendrite tip and root increases with increasing length of the interdendritic region that then requires a higher liquid flow rate in this region. A hot-crack may originate if this flow rate is not met [73]. Suppressed columnar growth leads to a reduced length of capillary channel existing between the dendrites. Subsequently, the pressure differential between the tip and root of a dendrite reduces and so does the alloy HCS [73]. Further, solute segregation induced changes in grain boundary energy and free surface energy may also affect HCS. To understand this, we formulated a theoretical framework using Rappaz, Jacot and Boettger's dendrite arm and grain coalescence model [38] and Rice and Wang's treatment of segregation-induced changes in grain boundary cohesion [35]. Naturally, to avoid intergranular cracking during solidification, grain bridging or coalescence must be promoted. Now, if γ_{SL} is the interfacial energy of the solid-liquid interface involving a grain and intergranular liquid, then prior to coalescing, the overall interfacial energy of a system of two adjacent grains with intergranular liquid in the channel between them would be $2\gamma_{SL}$. Upon complete solidification, the two solid/liquid interfaces coalesce, and the interfacial energy becomes equal to γ_{GB} . An attractive interaction occurs between the approaching solid/liquid interfaces when the total interfacial energy reduces as it becomes γ_{GB} from $2\gamma_{SL}$.

i.e., when $\gamma_{GB} < 2\gamma_{SL}$. Such attractive interaction between the interfaces is likely to promote coalescence or bridging of grains as the existence of intergranular liquid film becomes energetically unfavorable with reducing intergranular separation [37,38]. Conversely, for a repulsive interaction between the two solid/liquid interfaces, i.e., when $\gamma_{GB} > 2\gamma_{SL}$, the intergranular liquid film remains stable at lower temperatures, and thus, the alloy requires more undercooling before the grains could bridge to form a coherent solid network. Consequently, coalescence of the grains is delayed. Under such circumstances of delayed coalescence, at the terminal stage of solidification when liquid permeability of the solidifying network is already reducing (due to the increasing fraction of solid), the feeding of liquid into an opening in the mushy zone would now have to be performed until a much later stage during solidification and in a less permeable solid network. Naturally, the intergranular liquid film is not capable of effectively accommodating the shrinkage strains developing during solidification. Therefore, the intergranular cracking susceptibility of the alloy increases when the interaction is repulsive ($\gamma_{GB} > 2\gamma_{SL}$). Note that the increased undercooling required for coalescence of two grains implies that the alloy has a high CTR (described in Section 3.1). Now that the effect of interfacial energies, γ_{GB} and $2\gamma_{SL}$, on the alloy HCS has been discussed, we address the effect of solute segregation on these interfacial energies and subsequently, on the alloy HCS. For this, we first invoke the thermodynamic treatment of boundary cohesion and decohesion; this treatment is effective here because it correlates the boundary cohesion and decohesion with interfacial energies. Considering brittle fracture, the work of decohesion of grain boundaries per unit area for the pure metal, $(W_d)_{\Gamma=0}$, is given by Eq. (2) [28,74],

$$(W_d)_{\Gamma=0} = 2(\gamma_s)_{\Gamma=0} - (\gamma_{GB})_{\Gamma=0} \quad (2)$$

where $(\gamma_s)_{\Gamma=0}$ and $(\gamma_{GB})_{\Gamma=0}$ are the free surface energy per unit area and grain boundary energy per unit area for the pure metal, respectively. Γ represents solute concentration per unit area at the interface and equals zero for the pure metal. Upon alloying with a segregant, the work of decohesion of the grain boundaries per unit area, $(W_d)_{\Gamma}$, becomes

$$(W_d)_{\Gamma} = 2(\gamma_s)_{\Gamma} - (\gamma_{GB})_{\Gamma}, \quad (3)$$

where $(\gamma_s)_{\Gamma}$ and $(\gamma_{GB})_{\Gamma}$ are the free surface energy per unit area and grain boundary energy per unit area for the alloy, respectively. Upon alloying, the boundary decohesion is energetically favored when

$$(W_d)_{\Gamma} < (W_d)_{\Gamma=0}. \quad (4)$$

Using eq. (2), (3) and (4), we obtain the following condition for boundary decohesion to be energetically favored

$$2(\gamma_s)_{\Gamma} - (\gamma_{GB})_{\Gamma} < 2(\gamma_s)_{\Gamma=0} - (\gamma_{GB})_{\Gamma=0}. \quad (5)$$

Further rearrangement of (5) gives

$$2(\gamma_s)_{\Gamma} - 2(\gamma_s)_{\Gamma=0} < (\gamma_{GB})_{\Gamma} - (\gamma_{GB})_{\Gamma=0} \quad (6)$$

$$\text{or } \Delta\gamma_s < \Delta\gamma_{GB} \quad (7)$$

i.e., decohesion is energetically favored upon alloying when the change in free surface energy ($\Delta\gamma_s$) is lower than the change in the grain boundary energy ($\Delta\gamma_{GB}$). Similarly, it may be proved that the boundary cohesion is energetically favored when

$$\Delta\gamma_s > \Delta\gamma_{GB}. \quad (8)$$

Having discussed the thermodynamics of boundary cohesion and decohesion, we now address the effects of boundary segregation on γ_{GB} , γ_s , and overall, on the work of decohesion and alloy HCS. Eq. (9) represents the energetics of segregation-induced

changes in grain boundary cohesion. The reversible work of decohesion of a grain boundary is expressed as

$$(W_d)_\Gamma = [2(\gamma_S)_{\Gamma=0} - (\gamma_{GB})_{\Gamma=0}] - \int_0^\Gamma [\mu_{GB}(\Gamma) - \mu_S(\Gamma/2)] d\Gamma , \quad (9)$$

where μ_{GB} is the chemical potential of a grain boundary with segregant concentration Γ , and μ_S is the chemical potential of one of the two free surfaces (forming upon decohesion) with segregant concentration $\Gamma/2$. Rice and Wang [35,75] formulated that alloying elements that segregate towards free surfaces rather than unstressed grain boundaries, decrease the work of decohesion $(W_d)_{\Gamma < (W_d)_{\Gamma=0}}$ or cause boundary embrittlement, in that $\mu_{GB}(\Gamma) > \mu_S(\Gamma/2)$. On the other hand, alloying elements such as boron and carbon in iron, which segregate towards the unstressed grain boundaries, increase the work of decohesion $(W_d)_{\Gamma > (W_d)_{\Gamma=0}}$ or strengthen the grain boundaries. Therefore, alloying a pure metal with segregating elements alters its γ_{GB} , γ_S , and subsequently the work of decohesion (W_d) . In the case of solute segregation towards free surfaces and subsequent segregation induced embrittlement of the alloy, Eq. (5) is applicable. Evidently, a segregation-induced decrease in γ_S and increase in γ_{GB} leads to embrittlement, i.e., decreases W_d of the alloy. Note that a decrease in γ_S also means decrease in γ_{SL} , the two being related by Young's equation. Thus, segregation-induced decrease in γ_S and increase in γ_{GB} , promotes a repulsive type of interaction between the solidifying boundaries, in that γ_{SL} is also reduced. A repulsive interaction will naturally occur in the case when γ_S becomes less than γ_{GB} upon alloying, i.e., $(\gamma_S)_\Gamma < (\gamma_{GB})_\Gamma$. For such repulsive interaction, retention of the liquid film is energetically favored for a wider temperature range and subsequently, the coalescence of the boundaries may be delayed. Naturally, enhanced thermodynamic stability of the liquid film, and delayed coalescence also means that a greater undercooling would be required for the solidification to complete, i.e., the alloy would exhibit a high CTR. Thus, embrittling segregants may be detrimental to the alloy HCS. Conversely, a segregation-induced strengthening of grain boundaries (or put in another way, a segregation induced increase in W_d) that is led by an increase in γ_S and decrease in γ_{GB} , promotes an attractive type of interaction between the solidifying boundaries, in that the alloy may exhibit a high γ_{SL} . An attractive interaction will naturally occur in the case when γ_{GB} becomes less than γ_S upon alloying, i.e., $(\gamma_{GB})_\Gamma < (\gamma_S)_\Gamma$. For an attractive type of interaction, the coalescence of solidifying boundaries becomes more energetically favorable over retention of the thin liquid film between the boundaries. Thus, such attractive interaction fosters grain coalescence, and reduces the alloy HCS. Fig. 11 illustrates the effect of solute segregation on HCS of an alloy. Having discussed the effect of solute segregation on interfacial energies and alloy HCS, we now review the effect of segregation of Cr, Mn, and B on interfacial energies, and subsequently on alloy HCS. Although the interfacial energy of the boundaries may reduce with segregation of Cr, Mn, and B, Mn is known to cause decohesion, i.e., decrease W_d of the alloy [32,76]. Therefore, as per Rice-Wang's formulation, being the segregant of embrittling type, Mn may reduce the free surface energy. Further, a repulsive type of interaction between the solidifying boundaries will occur if $(\gamma_S)_\Gamma$ becomes less than $(\gamma_{GB})_\Gamma$ upon the addition of Mn. Conversely, Cr and B are strengthening type of segregants, and thus, will lead to an attractive interaction between the solidifying boundaries if $(\gamma_{GB})_\Gamma$ becomes less than $(\gamma_S)_\Gamma$ upon the addition of Cr and B.

4.2. Mechanical behavior (as-built specimens)

The excellent enhancement in strength of all as-built CS-BC specimens as compared to the as-built CS-HEA (Fig. 7(a), 7(c)) is

attributed to the MHH in the former that triggered multiple deformation mechanisms. In addition to solid solution strengthening, and Hall-Petch strengthening, particle strengthening arising from the nanoscale precipitates in CS-BC (Fig. 3(a)), would also contribute to the YS of as-built CS-BC. Further, a high density of intersecting stacking faults as observed in the as-built CS-BC 120-800 specimen (Fig. 4(b)) would also contribute to its YS [58,77]. Note that the contributors to these strengthening mechanisms create a microstructural hierarchy in CS-BC, in that they include solute atoms, dislocations including stacking faults, precipitates, and grain boundaries. A heterogeneity in grain size was also evident in as-built CS-BC 120-800 specimen (Fig. 2(c)). Such hierarchy and heterogeneity are important for storing a high density of geometrically necessary dislocations (GND) and, thus, for improving strength and WHR [78]. Elaborating, in alloys exhibiting MHH, several obstacles (spanning multiple length scales) to dislocation motion exist within the microstructure. The distance between two adjacent obstacles varies depending on the obstacle type; e.g., the distance between two adjacent stacking faults within a grain is of the order of nanometers (Fig. 4(b)), whereas that between two adjacent grain boundaries is within the sub-micrometer length scale. The smaller the distance between two obstacles, the more effective the obstacle is in obstructing dislocation motion [78]. Since several obstacles spanning multiple length scales exist within alloys exhibiting MHH, the effectiveness of these obstacles in obstructing dislocation motion also varies in these alloys. During deformation, such variation in obstacle effectiveness creates within the microstructure deformation gradients that must be accommodated by accumulation of GND. The accumulation of GND in turn produces back-stress (a long-range stress acting in a direction opposite to the applied shear stress) and inhibits further slip [7,78–80]. Steeper the deformation gradients, the higher is the GND density, the greater is the strengthening effect and higher is the WHR. A very high initial WHR of CS-BC 120-800 specimen as compared to the CS-HEA (Fig. 7(b)) evidences that the MHH in CS-BC could store a high density of GND in the initial stage of plastic deformation (for strain < 4%). However, beyond ~ 4% strain, the WHR of CS-BC falls below that of CS-HEA; this indicates that dynamic recovery occurred in CS-BC at a relatively early stage during plastic deformation [81]. In contrast, CS-HEA exhibits a moderate yet sustained WHR in Stage III (sustained between 2000–3000 MPa) and thus a high EF (~24.6%) as compared to the as-built CS-BC (~5.6%). Comparison of phase fractions in undeformed (Fig. 2(g)) and deformed conditions (Fig. 7(a)) of CS-HEA confirms that such sustained WHR until later stages of deformation in CS-HEA arises from its highly metastable γ -f.c.c. phase that undergoes deformation-induced phase transformation and subsequently produces TRIP effect. Further, the ϵ -h.c.p. phase in CS-HEA is known to deform by twinning and non-basal slip [82,83]. Thus, a sustained WHR and multiple deformation mechanisms in ϵ phase in CS-HEA result in its high ductility as compared to the as-built CS-BC specimens. Additionally, the undissociated B_4C particles may also be responsible for reduced ductility of CS-BC. Supplementary Fig. S4 shows one such undissociated B_4C particle. A discussion on the enhanced stability of γ phase and suppressed TRIP effect in as-built CS-BC specimens is provided in the next section. Notably, while the as-built CS-HEA exhibited deformation features in the form of dislocations, stacking faults, and twins (Fig. 4(a)), the as-built CS-BC exhibited only stacking faults (Fig. 4(b)). The dislocation density in additively manufactured alloys may approach the dislocation density in heavily deformed alloys. During L-PBF, the alloy experiences thermal strains. The variation in solidification parameters (thermal gradient and growth rate) and the subsequent variation in cooling rate across the melt pool [1,84] contributes to development of these thermal strains in L-PBF processed alloys. Further, heat is rejected from the upper layers towards the bottom layers; thus, a region

within the build may experience repeated tension-compression cycles [85]. Such inherent process dynamics of L-PBF lead to high dislocation densities within the L-PBF processed alloys. While the CS-HEA may accommodate this thermomechanical process-induced deformation through phase transformation, generation of dislocations, stacking faults, and/or twins, the CS-BC may accommodate this deformation only through generation of dislocations and stacking faults due to its relatively higher stacking fault energy. Origin of higher stacking fault energy of CS-BC is discussed in the next section.

In as-built CS-BC specimens, a trend of high YS in specimens processed at slow scanning speed and lower laser power is observed (Fig. 7(c)). Such a trend is ascribed to formation of a smaller melt pool volume that cools at a faster rate in these specimens [86]. A faster cooling rate in turn results in microstructural refinement (Fig. 6) and thus, high YS (Fig. 7(c)). Interestingly, specimen 120-800, which exhibited a wider distribution of grain size (Fig. 6), also exhibited good synergistic strength-ductility along with a high work-hardening rate (Fig. 7(c)). Such heterogeneous grain structured materials contain domains of soft regions (coarse grains) and hard regions (fine grains). The domain interfaces can then pile up GND and lead to high and sustained WHR and, thus, high synergistic strength and ductility [79].

4.3. Implications of annealing on segregation behavior, phase stability and mechanical behavior

The increased stability of γ phase within as-built CS-BC specimens as compared to the as-built CS-HEA specimen (Table 3) is associated with retention of C in solid solution in the former. C has higher solubility in γ -f.c.c. as compared to B and thus, B segregates towards the cell boundaries, whereas C is retained in the solid solution under conditions of rapid solidification in L-PBF (Fig. 3(b)-(c)). C can be accommodated within the interstitial γ -f.c.c. lattice sites due to its small size. Conversely, B atom has a peculiar size; it is too big to be accommodated within interstitial sites and too small to be accommodated within a substitutional site of a γ lattice [48]. Therefore, a high extent of misfit of a B atom leads to its high segregation tendency. Upon annealing, the $\gamma \rightarrow \epsilon$ phase transformation was evident in the CS-BC 120-800 specimen (Fig. 8(c)). Such phase transformation is attributed to depletion of C from the solid solution and its segregation at cell and grain boundaries to form the second-phase particles (Fig. 9(d)). Those cells and grains where depletion of C from solid solution occurred to form these particles transformed into ϵ phase (Fig. 8(b)-(c)). Therefore, the annealed CS-BC 120-800 specimen exhibited a dual-phase heterogeneity. Note that although the as-built CS-HEA exhibits such dual-phase heterogeneity with ϵ -dominant microstructure (Fig. 2(g)), the C-containing annealed CS-BC still exhibits a γ -dominant microstructure (Fig. 8(c)), which makes it amenable to a prominent TRIP effect.

Stacking fault energy (SFE) is known to influence the deformation mechanisms in alloys. Generally, with increasing SFE, the deformation mechanisms in f.c.c. alloys change from deformation-induced transformation to twinning induced plasticity (TWIP) to dislocation slip [58,59,87]. C is known to increase the SFE and enhance the stability of γ -f.c.c [55–59]. Eq. 10 relates SFE per unit area of fault (γ_{SFE}) to the change in free energy associated with $\gamma \rightarrow \epsilon$ transformation ($\Delta G_{\gamma \rightarrow \epsilon}$) [88],

$$\gamma_{SFE} = n\rho\Delta G_{\gamma \rightarrow \epsilon} + n\sigma_{\gamma/\epsilon} \quad (10)$$

where n represents the thickness of stacking fault in terms of number of planes, ρ is the planar density of atoms in close packed plane, and $\sigma_{\gamma/\epsilon}$ is the interfacial energy of the γ/ϵ interface. Thus, as C was retained in the solid solution within as-built CS-BC specimens, their SFE may have increased and may have led to sup-

pressed deformation induced $\gamma \rightarrow \epsilon$ transformation as well as suppressed TRIP effect. On the other hand, the carbon-free CS-HEA has a low SFE and thus is highly metastable, as reported in our recent work [59]. Subsequently, the TRIP effect is evident within the CS-HEA (Fig. 7(a)-(b)). However, as the CS-BC 120-800 specimen was annealed, C segregated to the cell and grain boundaries to form second-phase particles (Fig. 9(d)). With the depletion of C from solid solution, the SFE of γ phase in annealed specimen may have reduced and thus the metastability of γ phase was regained. This is manifested by significant deformation-induced $\gamma \rightarrow \epsilon$ transformation within the annealed specimen as evident upon comparison of phase fractions in undeformed (Fig. 8(c)) and deformed conditions (Fig. 10(c)). Several works have reported increase in SFE of γ -f.c.c.-containing alloys with increasing C content [55–57]; in addition, Seol et al. [70] demonstrated austenite to ferrite transformation with formation of carbides. The present observations are consistent with the literature-based expectations.

On one hand, hierarchical and heterogeneous microstructure consisting of solid solution, closely spaced stacking faults, precipitates, grain boundaries, and phase boundaries can store a high density of GND and, thus, contribute to the high YS of the annealed CS-BC specimen. On the other hand, a high and sustained WHR (sustained between ~ 4000 – 6000 MPa, Fig. 10(b)) resulting from such MHH and the metastable nature of phases, lead to high UTS and enhanced ductility of CS-BC in annealed condition (Fig. 10(a)) as compared to that in as-built condition (Fig. 7(a)). Note that the WHR in annealed CS-HEA is sustained between 4000 – 6000 MPa (Fig. 10(b)), whereas that in as-built CS-HEA is sustained between 2000 – 3000 MPa (Fig. 7(b)). This is explained on the basis of MHH and how pronounced the TRIP effect is in the two alloys [82]. The γ/ϵ ratio in annealed CS-BC (~ 1.86 , Fig. 8(c)) is much higher than that in as-built CS-HEA (~ 0.35 , Fig. 2(g)); however, the fraction of γ transformed upon deformation (ratio of change in γ phase fraction upon deformation to the initial γ phase fraction) does not differ significantly in the two alloys (0.60 in the former (Fig. 10(c)) and 0.62 in the latter (Fig. 7(a))). In the initial stages of plastic deformation, the enhanced MHH in the annealed CS-BC stores a higher density of GND as compared to the CS-HEA and results in a high initial WHR. On the other hand, beyond 2% strain, a high and sustained WHR in annealed CS-BC is attributed to the larger amount of γ phase available for deformation induced transformation as compared to the CS-HEA.

The as-built CS-BC specimen exhibited Mn segregation at the cell boundaries (Fig. 3), however, such Mn-enriched cell boundaries were not observed in the annealed CS-BC specimen (Fig. 9). While Cr segregation is known to impart a little to positive effect on boundary cohesion, Mn is an embrittling type of segregant in Fe-based alloys [31,32,76]. In addition to exhibiting Mn-segregation, the as-built CS-BC exhibited reduced metastability of γ -f.c.c. phase due to retention of C. Naturally, the reduced γ phase metastability suppressed the TRIP effect within the as-built CS-BC HEA. Further, a few undissociated B_4C particles were also observed in the as-built CS-BC HEA (supplementary Fig. S4). Thus, Mn segregation, reduced γ phase metastability, and presence of undissociated B_4C particles are the possible causes of a decreased EF of as-built CS-BC HEA as compared to the as-built CS-HEA. Note that the CS-HEA also exhibited Mn segregation at the cell boundaries (supplementary Fig. S6), however, its γ phase was highly metastable and it did not consist of B_4C particles. Upon annealing, as the cell boundaries were no longer enriched in Mn, and as depletion of C from solid solution occurred, the EF was enhanced. However, the EF of annealed CS-BC HEA still remained less than that of the as-built CS-HEA due to the presence of undissociated B_4C particles in the former. The B_4C particles remain undissociated after L-PBF processing and are likely to remain undissociated after annealing at 900°C – 10 mins. At ~ 6 μm in size, these particles are stress concen-

tration sites during tensile loading and may cause premature failure in the CS-BC HEA. Nonetheless, the detrimental effect of such particles on the tensile ductility of CS-BC HEA was significantly reduced with activation of TRIP effect in the annealed specimen.

Notably annealing reveals important information about the dissimilar segregation behaviors of solute elements in CS-HEA and CS-BC HEA. Evidently, CS-HEA exhibited segregation of Mn and Si; however, the segregation of Cr was not seen in as-built CS-HEA (supplementary Fig. 6); this result is consistent with low partition coefficient of Mn and Si and a relatively higher partition coefficient of Cr [89]. On the other hand, in as-built CS-BC, the segregation of Mn, Cr, and B was evident at the cell boundaries and Si was also seen segregating in the vicinity of the cell boundaries, as shown in Fig. 3. The difference in segregation behaviors of Cr in as-built CS-HEA and CS-BC is attributed to high tendency of Cr to form borides [67]. In the undoped CS-HEA, since B was not present, Cr did not exhibit any boundary segregation, whereas in the B₄C doped CS-HEA, as B segregated towards the cell boundaries, Cr also tended to segregate and form borides. However, the rapid solidification rate induced small diffusion distance in L-PBF AM allowed formation of only a limited volume fraction of borides (Fig. 3(a)). Further, within the as-built CS-BC specimen, the solute segregation was observed at the cell boundaries; during solidification in L-PBF, as these boundaries become enriched in solute, the undercooling in these regions may reach high values [1]. Such high undercooling also hinders the diffusional kinetics of formation of precipitates. Conversely, under equilibrium conditions of annealing, a relatively high-volume fraction of chromium borides was formed at the cell boundaries of the annealed CS-BC HEA (Fig. 9(a)). However, the EDS maps from the region showing cell boundary precipitation in the annealed specimen did not reveal Mn-rich zones (Fig. 9(f)). Therefore, it is evident that Cr exhibits a higher tendency to form borides and that its segregation depends on the B content (0 or 0.5 wt.%) as well as processing conditions (rapid solidification or annealing); this explains the higher segregation tendency of Cr in B-containing CS-BC HEA as compared to the B-free CS-HEA.

4.4. Alloy design considerations: outlook and prospects on segregation engineering of boundaries with L-PBF

4.4.1. Grain boundary segregation and alloy design considerations for solidification behavior during L-PBF

Rapid solidification in L-PBF proceeds by rejection of solute towards the dendritic and/or cellular boundaries. In any ternary or a higher order multicomponent alloy system, few solute atoms will have a higher tendency to segregate at the boundaries than others. Such tendency of an alloying element has been measured by the grain boundary enrichment factor (β), which is the ratio of effective concentration of the solute at the grain boundary to the concentration of solute in the bulk; β has been shown to increase with a decreasing solid solubility of the alloying elements [40,53]. Further, based on their effect on boundary strength, solute atoms can be categorized as either *strengthening* or *embrittling* [27]. Parameters including size of solute atoms [28,90], bond type and energy [52,91], and ratio of the surface energy of solute to that of solvent [31], have been used to determine if the solute atom is of strengthening or embrittling type. Few efforts have mapped such strengthening and embrittling tendencies of various solute atoms in different alloy systems [92,93]. Therefore, in addition to the cracking susceptible columnar growth naturally occurring in L-PBF, the solute atoms that embrittle the boundaries and have a high tendency to segregate at the boundaries may have a detrimental effect on the HCS of the alloy and, thus, on its printability and processing window. For such reasons, considering the segregating and strengthening/embrittling tendencies of the alloying elements while designing alloys for L-PBF is important. Further, a segregat-

ing solute may form boundary precipitates that may reduce boundary energy and retard boundary mobility through pinning. Such pinning effects may suppress columnar growth and thus reduce HCS of the alloy. Note that the pinning effects will be controlled by volume fraction and size of the pinning precipitates. The stage of solidification during L-PBF in which these precipitates form would determine the size of these precipitates and, thus, their effectiveness in suppressing columnar growth. Prediction of solidification path through computational tools is useful in this regard. Succinctly, dendritic solidification completes in three stages: Stage 1, where the dendrites are formed; Stage 2, which is marked by the coarsening of dendrites; and Stage 3, or the terminal stage, where the dendrites develop into grains and bridging occurs between two adjacent grains [62]. Since the coarsening of particles nucleating in a slurry or a mush is mediated by diffusion in the liquid [94], the formation of pinning particles when the majority of the matrix is in solid phase may prevent coarsening of these particles. However, formation of pinning phases at a later stage of solidification must also be considered; e.g., the terminal stage ($F_s > 0.9$ in Fig. 1(a)), may allow thermal gradient effects to take over before the pinning phases form and thus result in favorably oriented columnar growth (along <100> directions for cubic materials). Therefore, the pinning phases must form during Stage 2 of solidification, which is when the dendrites begin to coarsen [62]. However, care must be taken when assessing the embrittling nature of the pinning precipitates.

4.4.2. Grain boundary segregation and alloy design considerations for microstructure and mechanical behavior of L-PBF-processed alloy

Naturally, in addition to affecting solidification behavior, boundary segregation affects the mechanical properties of the L-PBF processed alloy, as described in the preceding sections of this work. Therefore, considering the effects of boundary segregation on mechanical properties of the alloy becomes vital to alloy design for L-PBF. At the outset, any embrittling alloying element would lead to poor structural integrity of the L-PBF processed component, in that the component may contain hot cracks. For an alloying element of strengthening type, the segregated solute atoms would lead to stabilization of fine-grained microstructure and would add to the strength of the boundaries and MHH of the alloy, whereas the pinning precipitates that may form during solidification would add to the alloy MHH. Enhanced MHH would allow storing high density of GNDs and thus contribute to high strength. Additionally, the formation of boundary precipitates may lead to a stable microstructure at high temperatures; however, attention must be paid to the embrittling effects (if any) of the boundary precipitates. As a secondary effect, a segregating alloying element of strengthening type may be added such that it alters the SFE of the alloy; this consideration is important from the viewpoint of activation of multiple deformation mechanisms. The deformation mechanisms in f.c.c. alloys may change with SFE as also discussed in Section 4.3 [58,59,87]. Using the findings shown in this work as an example, several deformation mechanisms could be activated in CS-BC. In as-built condition, as C was retained in solid solution, stacking faults, precipitates, and solid solution contributed to the high YS. Upon annealing, the boundary precipitates, stacking faults, dual phase microstructure and TRIP effect contributed to strength and ductility.

4.4.3. Implications of a wide L-PBF processing window of an alloy

With the addition of alloying elements of strengthening type, as columnar growth is suppressed and grain boundary cohesion improves, the alloy processing window with L-PBF is widened. Such widened processing window has significant implications in structural design, where the microstructural requirements of a component often vary with structural applications; e.g., a component

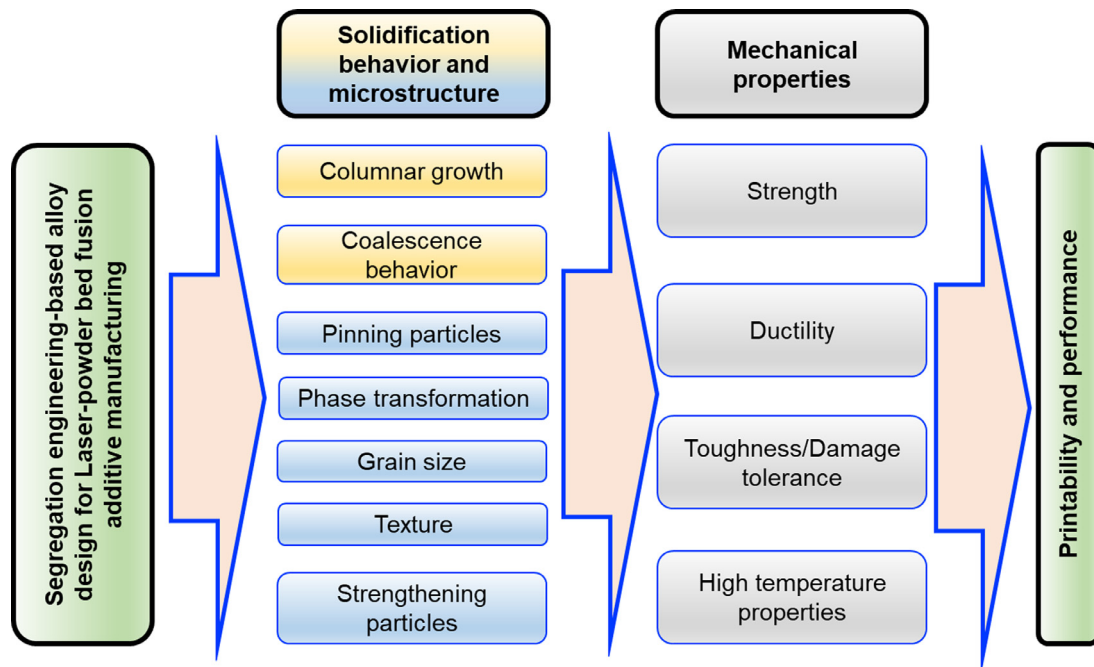


Fig. 12. Segregation affects alloy solidification behavior, the microstructure, and mechanical properties. Alloy design strategies that consider the effect of segregation on alloy solidification behavior, microstructure, and mechanical properties may lead to alloys that exhibit good printability and high application-specific performance with L-PBF additive manufacturing.

for high-temperature applications requires a thermally stable microstructure with pinning precipitates and coarse grains, whereas a component for high room temperature strength applications requires fine grains and activation of multiple strengthening mechanisms for high YS [95,96]. To meet the microstructural requirements of a structural application, the solidification parameters G and R may be varied by selection of appropriate process parameters in L-PBF; e.g., a high laser power results in low G , whereas a high scanning speed results in high R . Note that G and R control morphology and size of the microstructural features. Therefore, an alloy that exhibits a wide processing window may be processed at different L-PBF process parameters and, subsequently, may be used for application-specific manufacture. Using the findings shown in this work as an example, a wide crack-free processing window of CS-BC (Fig. 5) allowed exploiting the capability of L-PBF to control thermal gradients, growth rates and subsequently the cooling rate by altering the process-parameters, namely laser power and scan speed. Therefore, fine-tuning the attributes of microstructural heterogeneity, in this case heterogeneity of grain size, became possible (Fig. 6). Such microstructural fine-tuning allowed fine-tuning of the mechanical behavior (Fig. 7(c)); this is a step towards application-specific manufacture of an alloy with L-PBF. Fig. 12 outlines the key elements of an alloy design strategy for L-PBF that considers the effects of segregation on solidification behavior, microstructure, and mechanical properties of the alloy. The arrows depict the cause-effect relationships between and among segregation-based alloy design considerations, solidification behavior, microstructure, mechanical properties, alloy printability and performance.

5. Conclusions

Despite the prevalence of solute segregation in cellular and dendritic growth modes occurring in laser-powder bed fusion, the effects of solute segregation on solidification behavior of L-PBF-processed alloys are widely unknown. In this work, the effects of

solute segregation on L-PBF solidification behavior, microstructure, and mechanical properties of a 0.5 wt.% B_4C -doped metastable $F_{40}Mn_{20}Co_{20}Cr_{15}Si_5$ high entropy alloy were investigated.

Boron and carbon have high tendencies to segregate at the grain boundaries and to enhance grain boundary cohesion. Consequently, the as-built CS-BC evidenced boron segregation at the cell boundaries. As compared to the as-built CS-HEA, the as-built CS-BC exhibited suppressed columnar growth, suppressed cubic texture, finer cell size, and γ -f.c.c.-dominant microstructure. Further, the solid solution, stacking faults, precipitates, and varying grain size constituted microstructural heterogeneity and hierarchy within the as-built CS-BC. Such MHH led to increased yield strength (>1 GPa) and very high work hardening rate of as-built CS-BC. However, the retention of C in solid solution stabilized γ phase and suppressed the transformation induced plasticity effect in CS-BC.

A wide crack-free processing window of CS-BC allowed fine-tuning of its MHH and thus mechanical properties. A theoretical framework formulated to understand the effects of solute segregation on alloy HCS during L-PBF reveals that alloying elements that enhance grain boundary cohesion may also facilitate grain coalescence during solidification, prevent hot-cracking and therefore may widen crack-free L-PBF processing window of the alloy.

Upon annealing the CS-BC, carbon-rich precipitates formed at the cell and grain boundaries and reestablished the metastability of γ -f.c.c. phase. Such metastability was manifested by TRIP effect during tensile deformation. As compared to the as-built CS-HEA, the annealed CS-BC exhibited higher strength and a higher and sustained WHR. Further, a γ -dominant yet metastable microstructure of annealed CS-BC led to a pronounced TRIP effect.

A synergy of wide crack-free processing window and MHH allow application-specific manufacture with L-PBF in that the microstructure and thus the mechanical properties can be fine-tuned as per the requirements of the structural application. Such alloy design strategies may extend the outreach of fusion-based additive manufacturing processes to a wide range of structural applications.

Declaration of Competing Interest

None

CRediT authorship contribution statement

Saket Thapliyal: Conceptualization, Methodology, Investigation, Data curation, Formal analysis, Writing – original draft. **Priyanshi Agrawal:** Methodology, Writing – review & editing. **Priyanka Agrawal:** Methodology, Formal analysis, Writing – review & editing. **Saurabh S. Nene:** Methodology, Writing – review & editing. **Rajiv S. Mishra:** Funding acquisition, Conceptualization, Supervision, Resources, Writing – review & editing. **Brandon A. McWilliams:** Project administration, Writing – review & editing. **Kyu C. Cho:** Project administration, Writing – review & editing.

Acknowledgments

The study was performed under the cooperative agreement between University of North Texas and CCDC Army Research Laboratory ([W911NF1920011](#)). The authors thank Center for Agile and Adaptive Additive Manufacturing, Materials Research Facility (MRF) and Advanced Materials and Manufacturing Processes Institute (AMMPI) at University of North Texas for access to additive manufacturing equipment, electron microscopy and X-ray microscopy facilities, respectively.

Supplementary materials

Supplementary material associated with this article can be found, in the online version, at doi:[10.1016/j.actamat.2021.117271](#).

References

- [1] R.S. Mishra, S. Thapliyal, Design approaches for printability-performance synergy in Al alloys for laser-powder bed additive manufacturing, *Mater. Des.* (2021) 109640, doi:[10.1016/j.matdes.2021.109640](#).
- [2] R.S. Mishra, S.S. Nene, M. Frank, S. Sinha, K. Liu, S. Shukla, Metastability driven hierarchical microstructural engineering: Overview of mechanical properties of metastable complex concentrated alloys, *J. Alloys Compd.* 842 (2020) 155625, doi:[10.1016/j.jallcom.2020.155625](#).
- [3] R.S. Mishra, R.S. Haridas, P. Agrawal, High entropy alloys – Tunability of deformation mechanisms through integration of compositional and microstructural domains, *Mater. Sci. Eng. A* 812 (2021) 141085, doi:[10.1016/j.msea.2021.141085](#).
- [4] S.S. Nene, M. Frank, P. Agrawal, S. Sinha, K. Liu, S. Shukla, R.S. Mishra, B.A. McWilliams, K.C. Cho, Microstructurally flexible high entropy alloys: Linkages between alloy design and deformation behavior, *Mater. Des.* 194 (2020) 108968, doi:[10.1016/j.matdes.2020.108968](#).
- [5] J.W. Yeh, Physical Metallurgy of High-Entropy Alloys, *Jom* 67 (2015) 2254–2261, doi:[10.1007/s11837-015-1583-5](#).
- [6] Y. Brif, M. Thomas, I. Todd, The use of high-entropy alloys in additive manufacturing, *Scr. Mater.* 99 (2015) 93–96, doi:[10.1016/j.scriptamat.2014.11.037](#).
- [7] S. Shukla, D. Choudhuri, T. Wang, K. Liu, R. Wheeler, S. Williams, B. Gwalani, R.S. Mishra, Hierarchical features infused heterogeneous grain structure for extraordinary strength-ductility synergy, *Mater. Res. Lett.* 6 (2018) 676–682, doi:[10.1080/21663831.2018.1538023](#).
- [8] S. Shukla, T. Wang, S. Cotton, R.S. Mishra, Hierarchical microstructure for improved fatigue properties in a eutectic high entropy alloy, *Scr. Mater.* 156 (2018) 105–109, doi:[10.1016/j.scriptamat.2018.07.022](#).
- [9] W. Wu, R. Zhou, B. Wei, S. Ni, Y. Liu, M. Song, Nanosized precipitates and dislocation networks reinforced C-containing CoCrFeNi high-entropy alloy fabricated by selective laser melting, *Mater. Charact.* 144 (2018) 605–610, doi:[10.1016/j.matchar.2018.08.019](#).
- [10] E. Ma, T. Zhu, Towards strength-ductility synergy through the design of heterogeneous nanostructures in metals, *Mater. Today* 20 (2017) 323–331, doi:[10.1016/j.matto.2017.02.003](#).
- [11] P. Sathiyamoorthi, H.S. Kim, High-entropy alloys with heterogeneous microstructure: Processing and mechanical properties, *Prog. Mater. Sci.* (2020) 100709, doi:[10.1016/j.pmatsci.2020.100709](#).
- [12] Z.G. Zhu, Q.B. Nguyen, F.L. Ng, X.H. An, X.Z. Liao, P.K. Liaw, S.M.L. Nai, J. Wei, Hierarchical microstructure and strengthening mechanisms of a CoCrFeNiMn high entropy alloy additively manufactured by selective laser melting, *Scr. Mater.* 154 (2018) 20–24, doi:[10.1016/j.scriptamat.2018.05.015](#).
- [13] R. Li, P. Niu, T. Yuan, P. Cao, C. Chen, K. Zhou, Selective laser melting of an equiatomic CoCrFeMnNi high-entropy alloy: Processability, non-equilibrium microstructure and mechanical property, *J. Alloys Compd.* 746 (2018) 125–134, doi:[10.1016/j.jallcom.2018.02.298](#).
- [14] P.D. Niu, R.D. Li, T.C. Yuan, S.Y. Zhu, C. Chen, M.B. Wang, L. Huang, Microstructures and properties of an equimolar AlCoCrFeNi high entropy alloy printed by selective laser melting, *Intermetallics* 104 (2019) 24–32, doi:[10.1016/j.intermet.2018.10.018](#).
- [15] S. Luo, P. Gao, H. Yu, J. Yang, Z. Wang, X. Zeng, Selective laser melting of an equiatomic AlCrCuFeNi high-entropy alloy: Processability, non-equilibrium microstructure and mechanical behavior, *J. Alloys Compd.* 771 (2019) 387–397, doi:[10.1016/j.jallcom.2018.08.290](#).
- [16] T. Fujieda, M. Chen, H. Shiratori, K. Kuwabara, K. Yamanaka, Y. Koizumi, A. Chiba, S. Watanabe, Mechanical and corrosion properties of CoCrFeNiTi-based high-entropy alloy additive manufactured using selective laser melting, *Addit. Manuf.* 25 (2019) 412–420, doi:[10.1016/j.addma.2018.10.023](#).
- [17] S. Thapliyal, S.S. Nene, P. Agrawal, T. Wang, C. Morpheu, R.S. Mishra, B.A. McWilliams, K.C. Cho, Damage-tolerant, corrosion-resistant high entropy alloy with high strength and ductility by laser powder bed fusion additive manufacturing, *Addit. Manuf.* 36 (2020) 101455, doi:[10.1016/j.addma.2020.101455](#).
- [18] P. Agrawal, S. Thapliyal, S.S. Nene, R.S. Mishra, B.A. McWilliams, K.C. Cho, Excellent strength-ductility synergy in metastable high entropy alloy by laser powder bed additive manufacturing, *Addit. Manuf.* 32 (2020) 101098, doi:[10.1016/j.addma.2020.101098](#).
- [19] W. Kurz, C. Bezençon, M. Gäumann, Columnar to equiaxed transition in solidification processing, *Sci. Technol. Adv. Mater.* 2 (2001) 185–191, doi:[10.1016/S1468-6996\(01\)00047-X](#).
- [20] W. Kurz, D.J. Fisher, Fundamentals of Solidification, 4th ed., Trans Tech Publications Limited, 1998 <https://books.google.com/books?id=bFaxDwAAQBAJ>.
- [21] A. Basak, S. Das, Epitaxy and microstructure evolution in metal additive manufacturing, *Annu. Rev. Mater. Res.* 46 (2016) 125–149, doi:[10.1146/annurev-matsci-070115-031728](#).
- [22] D.G. Eskin, L.Katgerman Suyitno, Mechanical properties in the semi-solid state and hot tearing of aluminium alloys, *Prog. Mater. Sci.* 49 (2004) 629–711, doi:[10.1016/S0079-6425\(03\)00037-9](#).
- [23] Z. Sun, X.P. Tan, M. Descoings, D. Mangelinck, S.B. Tor, C.S. Lim, Revealing hot tearing mechanism for an additively manufactured high-entropy alloy via selective laser melting, *Scr. Mater.* 168 (2019) 129–133, doi:[10.1016/j.scriptamat.2019.04.036](#).
- [24] R. Zhou, Y. Liu, C. Zhou, S. Li, W. Wu, M. Song, B. Liu, X. Liang, P.K. Liaw, Microstructures and mechanical properties of C-containing FeCoCrNi high-entropy alloy fabricated by selective laser melting, *Intermetallics* 94 (2018) 165–171, doi:[10.1016/j.intermet.2018.01.002](#).
- [25] L. Zhou, H. Hyer, S. Thapliyal, R.S. Mishra, B. McWilliams, K. Cho, Y. Sohn, Process-dependent composition, microstructure, and printability of Al-Zn-Mg and Al-Zn-Mg-Sc-Zr Alloys manufactured by laser powder bed fusion, *Metall. Mater. Trans. A* (2020), doi:[10.1007/s11661-020-05768-3](#).
- [26] J.H. Martin, B.D. Yahata, J.M. Hundley, J.A. Mayer, T.A. Schaedler, T.M. Pollock, 3D printing of high-strength aluminium alloys, *Nature* 549 (2017) 365–369, doi:[10.1038/nature23894](#).
- [27] J.P. Hirth, J.R. Rice, On the thermodynamics of adsorption at interfaces as it influences decohesion, *Metall. Trans. A* 11 (1980) 1501–1511, doi:[10.1007/BF02654514](#).
- [28] M.P. Seah, Segregation and the strength of grain boundaries, *Proc. R. Soc. Lond. A. Math. Phys. Sci.* 349 (1976) 535–554 <http://www.jstor.org/stable/79009>.
- [29] E.D. Hondros, M.P. Seah, Theory of grain boundary segregation in terms of surface adsorption analogues, *Met. Trans. A* 8 A (1977) 1363–1371, doi:[10.1007/BF02642850](#).
- [30] A.D. Rollett, G. Gottstein, L.S. Shvindlerman, D.A. Molodov, Grain boundary mobility - a brief review, *Zeitschrift Fuer Met. Res. Adv. Tech.* 95 (2004) 226–229, doi:[10.3139/146.017938](#).
- [31] M.A. Gibson, C.A. Schuh, Segregation-induced changes in grain boundary cohesion and embrittlement in binary alloys, *Acta Mater.* 95 (2015) 145–155, doi:[10.1016/j.actamat.2015.05.004](#).
- [32] D. Raabe, M. Herbig, S. Sandlöbes, Y. Li, D. Tytko, M. Kuzmina, D. Ponge, P.P. Choi, Grain boundary segregation engineering in metallic alloys: a pathway to the design of interfaces, *Curr. Opin. Solid State Mater. Sci.* 18 (2014) 253–261, doi:[10.1016/j.cossms.2014.06.002](#).
- [33] J.W. Cahn, The impurity-drag effect in grain boundary motion, *Acta Metall.* 10 (1962) 789–798, doi:[10.1016/0001-6160\(62\)90092-5](#).
- [34] M. Hillert, B. Sundman, A treatment of the solute drag on moving grain boundaries and phase interfaces in binary alloys, *Acta Metall.* 24 (1976) 731–743, doi:[10.1016/0001-6160\(76\)90108-5](#).
- [35] J.R. Rice, J.S. Wang, Embrittlement of interfaces by solute segregation, *Mater. Sci. Eng. A* 107 (1989) 23–40, doi:[10.1016/0921-5093\(89\)90372-9](#).
- [36] M.P. Seah, Adsorption-induced interface decohesion, *Acta Metall.* 28 (1980) 955–962, doi:[10.1016/0001-6160\(80\)90112-1](#).
- [37] M. Rappaz, J.M. Drezet, P.D. Grasso, A. Jacot, Hot tearing and coalescence: Two deeply-connected phenomena, *Model. Cast. Weld. Adv. Solidif. Process.* (2003) 53–60.
- [38] M. Rappaz, A. Jacot, W.J. Boettinger, Last-stage solidification of alloys: Theoretical model of dendrite-arm and grain coalescence, *Metall. Mater. Trans. A Phys. Metall. Mater. Sci.* 34 A (2003) 467–479, doi:[10.1007/s11661-003-0083-3](#).
- [39] Z. Sun, X. Tan, C. Wang, M. Descoings, D. Mangelinck, S.B. Tor, E.A. Jägle, S. Zaeferer, D. Raabe, Reducing hot tearing by grain boundary segregation engineer-

- ing in additive manufacturing: example of an AlxCrFeNi high-entropy alloy, *Acta Mater.* 204 (2021) 116505, doi:10.1016/j.actamat.2020.116505.
- [40] M.P. Seah, E.D. Hondros, Grain boundary segregation, *Proc. R. Soc. Lond. A. Math. Phys. Sci.* 335 (1973) 191–212 <http://www.jstor.org/stable/78510>.
- [41] F. Liu, R. Kirchheim, Nano-scale grain growth inhibited by reducing grain boundary energy through solute segregation, *J. Cryst. Growth.* 264 (2004) 385–391, doi:10.1016/j.jcrysgr.2003.12.021.
- [42] T. Chookjorn, H.A. Murdoch, C.A. Schuh, Design of Stable Nanocrystalline Alloys, *Science* 337 (2012) 951 (80-.)LP –954, doi:10.1126/science.1224737.
- [43] J.B. Seol, J.W. Bae, Z. Li, J.Chan Han, J.G. Kim, D. Raabe, H.S. Kim, Boron doped ultrastrong and ductile high-entropy alloys, *Acta Mater.* 151 (2018) 366–376, doi:10.1016/j.actamat.2018.04.004.
- [44] E.D. Hondros, Segregation to interfaces, *Int. Met. Rev.* 22 (1977) 262–299, doi:10.1179/imtr.1977.22.1.1262.
- [45] X.L. He, Y.Y. Chu, J.J. Jonas, The grain boundary segregation of boron during isothermal holding, *Acta Metall.* 37 (1989) 2905–2916, doi:10.1016/0001-6160(89)90325-8.
- [46] D. Raabe, S. Sandlöbes, J. Millán, D. Ponge, H. Assadi, M. Herbig, P.P. Choi, Segregation engineering enables nanoscale martensite to austenite phase transformation at grain boundaries: A pathway to ductile martensite, *Acta Mater.* 61 (2013) 6132–6152, doi:10.1016/j.actamat.2013.06.055.
- [47] M.A.V. Chapman, R.G. Faulkner, Computer modelling of grain boundary segregation, *Acta Metall.* 31 (1983) 677–689, doi:10.1016/0001-6160(83)90083-4.
- [48] L. Karlsson, H. Norden, Non-equilibrium grain boundary segregation of boron in austenitic stainless steel, *Acta Metall.* 36 (1988) 35–48.
- [49] M. Kurban, U. Erb, K.T. Aust, A grain boundary characterization study of boron segregation and carbide precipitation in alloy 304 austenitic stainless steel, *Scr. Mater.* 54 (2006) 1053–1058, doi:10.1016/j.scriptamat.2005.11.055.
- [50] J.W. Gibbs, On the equilibrium of heterogeneous substances, *Am. J. Sci.* s3-16 (1878) 441–458, doi:10.2475/ajss.3-16.96.441.
- [51] C.M. Liu, T. Nagoya, K. Abiko, H. Kimura, Effect of boron on the grain boundary segregation of phosphorus and intergranular fracture in high-purity Fe-0.2 Pct P-B alloys, *Metall. Trans. A.* 23 (1992) 263–269, doi:10.1007/BF02660870.
- [52] R. Wu, A.J. Freeman, G.B. Olson, First-principles determination of the effects of phosphorus and boron on iron grain boundary cohesion, *Science* 265 (1994) 376–380 (80-.), doi:10.1126/science.265.5170.376.
- [53] E. Hondros, Boundary segregation: the current situation and future requirements, *J. Phys. Colloq.* 36 (1975) 117–135, doi:10.1051/j.physcol:1975413.
- [54] X.L. He, M. Djahazi, J.J. Jonas, J. Jackman, The non-equilibrium segregation of boron during the recrystallization of Nb-treated HSLA steels, *Acta Metall. Mater.* 39 (1991) 2295–2308, doi:10.1016/0956-7151(91)90012-P.
- [55] A. Abbasi, A. Dick, T. Hickel, J. Neugebauer, First-principles investigation of the effect of carbon on the stacking fault energy of Fe-C alloys, *Acta Mater.* 59 (2011) 3041–3048, doi:10.1016/j.actamat.2011.01.044.
- [56] A. Saeed-Akbari, J. Imlau, U. Prah, W. Bleck, Derivation and variation in composition-dependent stacking fault energy maps based on subregular solution model in high-manganese steels, *Metall. Mater. Trans. A Phys. Metall. Mater. Sci.* 40 (2009) 3076–3090, doi:10.1007/s11661-009-0050-8.
- [57] T.H. Lee, H.Y. Ha, B. Hwang, S.J. Kim, E. Shin, Effect of carbon fraction on stacking fault energy of austenitic stainless steels, *Metall. Mater. Trans. A Phys. Metall. Mater. Sci.* 43 (2012) 4455–4459, doi:10.1007/s11661-012-1423-y.
- [58] B.C. De Cooman, Y. Estrin, S.K. Kim, Twinning-induced plasticity (TWIP) steels, *Acta Mater.* 142 (2018) 283–362, doi:10.1016/j.actamat.2017.06.046.
- [59] M. Frank, Y. Chen, S.S. Nene, S. Sinha, K. Liu, K. An, R.S. Mishra, Investigating the deformation mechanisms of a highly metastable high entropy alloy using in-situ neutron diffraction, *Mater. Today Commun.* 23 (2020), doi:10.1016/j.mtcomm.2019.100858.
- [60] Y.F. Shen, X.X. Dong, X.T. Song, N. Jia, Carbon content-tuned martensite transformation in low-alloy TRIP steels, *Sci. Rep.* 9 (2019) 1–9, doi:10.1038/s41598-019-44105-6.
- [61] S. Thapliyal, M. Komarasamy, S. Shukla, L.Le Zhou, H. Hyer, S. Park, Y. Sohn, R.S. Mishra, An integrated computational materials engineering-anchored closed-loop method for design of aluminum alloys for additive manufacturing, *Materialia* 9 (2020) 100574, doi:10.1016/j.mtla.2019.100574.
- [62] B. Santillana, R. Boom, D. Eskin, H. Mizukami, M. Hanao, M. Kawamoto, High-temperature mechanical behavior and fracture analysis of a low-carbon steel related to cracking, *Metall. Mater. Trans. A Phys. Metall. Mater. Sci.* 43 (2012) 5048–5057, doi:10.1007/s11661-012-1331-1.
- [63] D.G. Eskin, L. Katgerman, Thermal contraction during solidification of aluminium alloys, *Mater. Sci. Forum.* 519–521 (2006) 1681–1686, doi:10.4028/www.scientific.net/msf.519-521.1681.
- [64] I.I. Novikov, Hot-shortness of Nonferrous Metals and Alloys, Defense Technical Information Center, 1968.
- [65] X. Chen, Y. Li, H. Zhang, Microstructure and mechanical properties of high boron white cast iron with about 4 wt% chromium, *J. Mater. Sci.* 46 (2011) 957–963, doi:10.1007/s10853-010-4840-6.
- [66] Z. Liu, X. Chen, Y. Li, K. Hu, High boron iron-based Alloy and its modification, *J. Iron Steel Res. Int.* 16 (2009) 37–54, doi:10.1016/S1006-706X(09)60041-8.
- [67] M.M. Gauthier, Crystallography and engineering properties of ceramics, *Eng. Mater. Handb. Des. Ed.* (1995) 0, doi:10.31399/asm.hb.emde.a0003059.
- [68] S.A. Khairallah, A.T. Anderson, A. Rubenchik, W.E. King, Laser powder-bed fusion additive manufacturing: Physics of complex melt flow and formation mechanisms of pores, spatter, and denudation zones, *Acta Mater.* 108 (2016) 36–45, doi:10.1016/j.actamat.2016.02.014.
- [69] B. Zhang, Y. Li, Q. Bai, Defect formation mechanisms in selective laser melting: a review, *Chinese J. Mech. Eng. (English Ed.)* 30 (2017) 515–527, doi:10.1007/s10033-017-0121-5.
- [70] J.B. Seol, N.S. Lim, B.H. Lee, L. Renaud, C.G. Park, Atom probe tomography and nano secondary ion mass spectroscopy investigation of the segregation of boron at austenite grain boundaries in 0.5 wt.% carbon steels, *Met. Mater. Int.* 17 (2011) 413–416, doi:10.1007/s12540-011-0617-y.
- [71] R. Kirchheim, Grain coarsening inhibited by solute segregation, *Acta Mater.* 50 (2002) 413–419, doi:10.1016/S1359-6454(01)00338-X.
- [72] A.D. Rollett, G. Gottstein, L.S. Shvindlerman, D.A. Molodov, Grain boundary mobility – a brief review, *Zeitschrift Für Met* 95 (2004) 226–229, doi:10.3139/146.017938.
- [73] M. Rappaz, J.M. Drezet, M. Gremaud, A new hot-tearing criterion, *Metall. Mater. Trans. A Phys. Metall. Mater. Sci.* 30 (1999) 449–455, doi:10.1007/s11661-999-0334-z.
- [74] M.C. Inman, H.R. Tipler, Interfacial energy and composition in metals and alloys, *Metall. Rev.* 8 (1963) 105–166, doi:10.1179/mtr.1963.8.1.105.
- [75] J.R. Rice, Effect of hydrogen on behavior of materials, *Metall. Soc. AIME.* (1976) 455–466 http://esag.harvard.edu/rice/060_Rice_HydrogenInterfaceCohes_AIME76.pdf.
- [76] R. Yang, D.L. Zhao, Y.M. Wang, S.Q. Wang, H.Q. Ye, C.Y. Wang, Effects of Cr, Mn on the cohesion of the γ -iron grain boundary, *Acta Mater.* 49 (2001) 1079–1085, doi:10.1016/S1359-6454(00)00382-7.
- [77] K. Yamana, M. Mori, S. Sato, A. Chiba, Stacking-fault strengthening of biomedical Co-Cr-Mo alloy via multipass thermomechanical processing, *Sci. Rep.* 7 (2017) 1–13, doi:10.1038/s41598-017-10305-1.
- [78] M.F. Ashby, The deformation of plastically non-homogeneous materials, *Philos. Mag.* 21 (1970) 399–424, doi:10.1080/14786437008238426.
- [79] X. Wu, Y. Zhu, Heterogeneous materials: a new class of materials with unprecedented mechanical properties, *Mater. Res. Lett.* 5 (2017) 527–532, doi:10.1080/21663831.2017.1342208.
- [80] N.A. Fleck, M.F. Ashby, J.W. Hutchinson, The role of geometrically necessary dislocations in giving material strengthening, *Scr. Mater.* 48 (2003) 179–183, doi:10.1016/S1359-6462(02)00338-X.
- [81] A.D. Rollett, U.F. Kocks, A Review of the Stages of Work Hardening, *Solid State Phenom.* 35–36 (1993) 1–18, doi:10.4028/www.scientific.net/sp.35-36.1.
- [82] S. Sinha, S.S. Nene, M. Frank, K. Liu, R.A. Lebensohn, R.S. Mishra, Deformation mechanisms and ductile fracture characteristics of a friction stir processed transformative high entropy alloy, *Acta Mater.* 184 (2020) 164–178, doi:10.1016/j.actamat.2019.11.056.
- [83] S. Sinha, S.S. Nene, M. Frank, K. Liu, P. Agrawal, R.S. Mishra, On the evolving nature of c/a ratio in a hexagonal close-packed epsilon martensite phase in transformative high entropy alloys, *Sci. Rep.* 9 (2019) 1–14, doi:10.1038/s41598-019-49904-5.
- [84] S. Thapliyal, S. Shukla, L. Zhou, H. Hyer, P. Agrawal, P. Agrawal, M. Komarasamy, Y. Sohn, R.S. Mishra, Design of heterogeneous structured Al alloys with wide processing window for laser-powder bed fusion additive manufacturing, *Addit. Manuf.* 42 (2021) 102002, doi:10.1016/j.addma.2021.102002.
- [85] G. Wang, H. Ouyang, C. Fan, Q. Guo, Z. Li, W. Yan, Z. Li, The origin of high-density dislocations in additively manufactured metals, *Mater. Res. Lett.* 8 (2020) 283–290, doi:10.1080/21663831.2020.1751739.
- [86] Q. Guo, C. Zhao, M. Qu, L. Xiong, L.I. Escano, S.M.H. Hojjatzaadeh, N.D. Parab, K. Fezzaa, W. Everhart, T. Sun, L. Chen, In-situ characterization and quantification of melt pool variation under constant input energy density in laser powder bed fusion additive manufacturing process, *Addit. Manuf.* 28 (2019) 600–609, doi:10.1016/j.addma.2019.04.021.
- [87] M.A. Meyers, M.S. Schneider, H. Jarmakanian, B. Kad, B.A. Remington, D.H. Kalantar, J. McNaney, B. Cao, J. Wark, Deformation substructures and their transitions in laser shock-compressed copper-aluminum alloys, *Metall. Mater. Trans. A Phys. Metall. Mater. Sci.* 39 (2008) 304–321, doi:10.1007/s11661-007-9359-3.
- [88] G.B. Olson, M. Cohen, A general mechanism of martensitic nucleation: Part I. General concepts and the FCC \rightarrow HCP transformation, *Metall. Trans. A* 7 (1976) 1897–1904, doi:10.1007/BF02659822.
- [89] T.P. Battle, R.D. Pehlke, Equilibrium partition coefficients in iron-based alloys, *Metall. Mater. Trans. B* 20 (1989) 149–160, doi:10.1007/BF02825596.
- [90] R. Schweinfest, A.T. Paxton, M.W. Finnis, Bismuth embrittlement of copper is an atomic size effect, *Nature* 432 (2004) 1008–1011, doi:10.1038/nature03198.
- [91] R.P. Messmer, C.L. Briant, The role of chemical bonding in grain boundary embrittlement, *Acta Metall.* 30 (1982) 457–467, doi:10.1016/0001-6160(82)90226-7.
- [92] M.A. Gibson, C.A. Schuh, A survey of ab-initio calculations shows that segregation-induced grain boundary embrittlement is predicted by bond-breaking arguments, *Scr. Mater.* 113 (2016) 55–58, doi:10.1016/j.scriptamat.2015.09.041.
- [93] P. Lejček, M. Šob, An analysis of segregation-induced changes in grain boundary cohesion in bcc iron, *J. Mater. Sci.* 49 (2014) 2477–2482, doi:10.1007/s10853-013-7943-z.
- [94] S. Takajo, W.A. Kaysser, G. Petzow, Analysis of particle growth by coalescence during liquid phase sintering, *Acta Metall.* 32 (1984) 107–113, doi:10.1016/0001-6160(84)90207-4.
- [95] P. Agrawal, S. Shukla, S. Thapliyal, P. Agrawal, S.S. Nene, R.S. Mishra, B.A. Mcwilliams, K.C. Cho, Microstructure-property correlation in a laser powder bed fusion processed high strength AF-9628 steel, *Adv. Eng. Mater.* (2020).
- [96] N. Kumar, R.S. Mishra, Additivity of strengthening mechanisms in ultrafine grained Al-Mg-Sc alloy, *Mater. Sci. Eng. A* 580 (2013) 175–183, doi:10.1016/j.msea.2013.05.006.